University of West Bohemia
Faculty of Electrical Engineering

DISSERTATION

Analytical Models for IGBT Junction Temperature Estimation

Humphrey Mokom, Njawah Achiri **Pilsen, 2022**

FACULTY OF ELECTRICAL
ENGINEERING
UNIVERSITY OF WEST BOHEMIA

Dissertation

to earn the academic degree Ph.D. in the field

Electronics / Electrical Power Engineering / Electrical Engineering

Humphrey Mokom, Njawah Achiri

Analytical Models for IGBT Junction Temperature Estimation

Supervisors: Zdenek, Peroutka, Prof
Vaclav Smidl, Assoc. Prof

Declaration

I declare that I have elaborated the dissertation thesis individually and have used sources which I cite and list in the bibliography. In the submitted scientific work the usual scientific procedures are used.

Plzeň, date

……

signature

Acknowledgments

I would like to thank my supervisors Prof. Peroutka and Assoc. Prof Smidl for their guiding me throughout this journey. I will also like to thank my wife Marilyn and my kids, Myiesha, Miriam and Bright for their emotional support as I embarked on this journey. Finally, I say thank you to the entire lab staff of RICE and everyone who contributed in one way or another to make this dream of mine come true.

Project leader's statement

I declare that within the XXX project, in which this dissertation thesis was elaborated, presented results were achieved. The student participated in these results by xx%.

Plzeň, date

……

signature

Abstract

A thermal model to accurately estimate the junction temperature of inverters is developed. State of the art methods for determining thermal impedance networks for IGBT modules are used in the establishment of the relationship between the measured transistor or diode voltage and temperature under homogenous temperature distribution across the IGBT module. The junction temperature is recomputed from the established voltage-temperature relationship and used in determining the thermal impedance network. These methods requires accurate measurement of voltage drop across the transistors and diodes under specific designed heating and cooling profiles. Validation of the junction temperature is done using infrared camera or sensors placed closed to the transistors or diodes (in some cases and open IGBT module) so that the measured temperature is as close to the junction as possible. In this thesis we propose an alternative method for determining the IGBT thermal impedance network using the principles of least squares. This method uses measured temperatures for defined heating and cooling cycles under different cooling conditions to determine the thermal impedance network. The results from the proposed method are compared with those obtained using state of the art methods. Based on the calculated junction temperature, an optimal thermal management strategy of the electric drivetrain based on adaptive linear current derating and I2t derating to allow for maximum possible torque and optimum thermal protection of the electric drivetrain is implemented.

List of Figures

List of Tables

Table of Contents

1. Introduction

1.1. Motivation

Due to increasing demands in power densities of automotive electric traction drives fuelled by limited space availability in the vehicle and performance requirements, engineers strive to obtain best possible performance from all traction drive components (inverters, DC-DC converters, electric machines). This means that the electric traction drive is thermally stressed especially during operation at high loads such driving off-road or in stop and go traffic situations. A safe operation near thermal limits of the components in these high load scenarios in necessary to obtain the required performance.

Pure silicon IGBT modules though widely used in automotive traction drive inverters still pose some thermal challenges. They have a very low thermal time constant and a relatively low allowed maximum operating junction temperature. Hence to safely operate these inverters under high load conditions, an accurate estimation of junction temperature is required. This thesis examines methods to accurately characterise he thermal impedance network of the IGBT module from which the junction temperature is estimated. Derating strategies to guarantee safe operation and optimum performance under high load operation are investigated.

1.2. Literature Review

Operation of inverters under peak load and frequent thermal transient conditions, require a precise estimation of the junction temperature for effective thermal management. These conditions are common in inverters used in automotive traction drives operating under low speed and high torque demands such as stop-and-go situations in city driving, off-road/uphill driving, or towing a trailer. In some cases, IGBT modules are equipped with temperature sensors. Typical sensors used usually have a slow thermal response [1] [2] and are much more suitable for measuring baseplate or case temperatures with high thermal time constants compared to the junction temperature. Even if much more accurate sensors or those with faster responses were to be used, a sensor will have to be placed closed to each diode or transistor in the IGBT module. During asymmetrical loading of the inverter, some transistors or diodes allow higher currents than others and consequently have higher temperatures. Hence depiction of individual diodes and transistor temperatures are necessary [3]. Placing sensors closed to each transistor or diode in an IGBT module increases the overall cost of the inverter and also presents some packaging challenges. In addition to effective real time thermal management and control of inverters [4] information about the junction temperature is imperative in the study of ageing and degradation of IGBT modules [5] [6] [7] [8] [9]. Such

studies provide vital information needed in implementing appropriate thermal management and control strategies of the inverter which limit frequent operation of the inverter in thermally critical temperature ranges thereby extending the lifetime of the IGBT module and consequently in overall life time of the inverter [10] [11] [12].

In the design of electric traction drives for automotive applications, key design considerations are cost, efficiency, weight and size. This is due to the limited amount of available space in the vehicle where downsizing of inverters as well as the overall electric drive has become inevitable. Small, lightweight and highly efficient inverters are expected to meet the ever increasing demands in power, performance comparable to or better than conventional gasoline powered vehicles. Thus high efficiency, low weight and low cost are key design considerations for electric traction drives [13] [14]. High power requirements also mean high thermal stress on the inverter since the inverter is operated mostly at high temperatures which lead to rapid aging of the inverter components [15].

Although Silicon Carbide SiC and other wide band gap devices offer significant performance improvements on the switching level [16], the technology is still too expensive for automotive applications and most automotive inverters are not operated very high frequencies where the advantages of wide band gap devices over pure silicon devices are dominant. Wide band gap devices also present challenges in availability of packaging technology to accommodate their high operating temperatures. Most state of the art pure silicon based devices (IGBT modules) have a maximum allowed junction temperature of 175°C [17] [18] and an operating junction temperature of 150°C for automotive certified IGBT modules [19] [20] [21]. With expected nominal coolant temperatures of 65 – 70°C for liquid cooled drivetrains (mixture of water/glycol 50 – 50 and coolant flow rate of between 6 to 10 litres per minute) [22] [3] only a maximum temperature buffer of 80°C is available to satisfy the vehicles peak power requirement. Wide band gap devices (Silicon Carbide SiC and Gallium Nitrate GaN) have generally low losses than pure silicon devices, high junction temperatures (theoretical junction temperatures of up to 700°C) and thus allow for high frequency operation (greater than 20 kHz) [17] [18].

Due to the limited temperature buffer between nominal coolant temperature and maximum operating inverter junction temperature, a very precise inverter junction temperature observer is required to accurately calculate the junction temperature for optimum thermal operation of the inverter (operating the inverter in the critical temperature range 140°C – 150°C at maximum possible torque). Junction temperature estimation typically stems from a model of the electro-thermal behaviour of the IGBT module. Typical models can be expressed a RC-circuits where resistances and capacitances represent the thermal impedances and capacitances of the individual elements (transistors and diodes) of the module. These RC-

circuits describe the heat transfer between the heat source and the heat sink. Two types of RC-circuit thermal networks are most frequently used in thermal modelling of an IGBT module; Foster network [3] [23] [24] and Cauer network [25] [26]. The type of network used usually dependents on the goal of the thermal model. The Cauer network is much more complex and provides detail information about intermediate temperatures of the different layers between the heat source and the heatsink which have a physical meaning.

Accurate online estimation of inverter junction temperature is fundamental in implementing a good thermal management strategy for the inverter to guarantee good thermal performance while protecting the inverter from excessive thermal stress which could either destroy the inverter or considerably reduce its overall lifetime. Analytical junction estimation techniques [27] [28] [29] [3] are widely used in industrial applications for online junction temperature estimation because it is not computational intensive and thus suitable for implementation on microcontroller. This technique makes use of a reference temperature which could be the measured heat sink or case temperature of the IGBT module together with a known thermal impedance between the reference temperature the junction temperature [28] [29] [3] [30] [31].

Most widely used methods in determining the thermal impedance of IGBT modules include finite element analysis (FEA) [32] [31] [33], direct temperature measurement using temperature sensors [34], infrared based temperature measurements [35] [9], the voltage-based thermo-sensitive electrical parameters (TSEP) approach [28] [36] [37] where the collector emitter voltage is measured at low currents during the cool down phase.

FEA models provide detailed results as the thermal impedance of each element along the path between the measured reference and junction temperature can be calculated. However, implementing a good FEA model to accurately obtain the required thermal impedances could prove to be a demanding task. Further, FEA models are based on ideal material properties which could provide a certain degree of inaccuracy in the results. FEA models are well suited to extraction of thermal impedance parameters but cannot be used for online estimation of junction temperature especially for arbitrary load profiles [32] due to their high required computation time.

To obtain accurate junction temperatures and consequently accurate thermal impedances from infrared as well as direct temperature measurements, the IGBT module has to be opened and the isolation gel washed out. In order to conduct measurements using the IR camera, the module has to be sprayed with a thermal spray. This thermal spray might affect the value of the measured temperature; hence the infrared camera has to be tuned after applying the spray [35]. Infrared measurements are advantageous in that provide a

complete temperature profile of the entire chip surface but have the disadvantage due to the fact that they can only be applied on open modules to measure the junction temperature.

The voltage-based TSEP method where the collector-emitter voltage or the forward voltage of the diode is measured at low currents is the most widely used method in determining thermal impedances. Using this method, the average junction temperature of the diode or IGBT is obtained [36]. This measurement method is easy to implement and can be conducted on closed as well as opened IGBT modules. However, discrepancies in measured results compared to those obtained using infrared measurements have been reported in [35].

Inverter power loss consists of switching and conduction losses. Strategies for increasing the power density of the inverter by reducing the switching frequency have been proposed in [38] [39]. Both strategies only work at low speed operation where the electrical output frequency of the drive is low. During high speed operation a high switching frequency is required to ensure controllability of the high electrical frequency of the resulting sinusoidal phase currents. Reducing the switching frequency also results in acoustic problem which could be unpleasant to the driver.

Inverter switching losses only account for about 30% of the total inverter loss, hence to safely operate the inverter, reduction of current is necessary when the junction temperature of inverter is above a system define safe operating threshold below which operation at full load under nominal cooling is allowed. This system defined threshold is usually limited by the maximum allowed operating junction temperature specified by the IGBT module manufacturer. State of the art or instantaneous derating strategies will reduce the current instantaneously when the temperature is above the predefined safe operating threshold.

A derating strategy is not only associated with safe operation of the electrical drive system. It also has a lot to do with the driving comfort because instantaneous current reduction may lead to drivetrain oscillations [40] [41] as shown in Figure 1. In [40] the authors focused on operating at or close to the thermal limits of the electrical drive without exceeding the thermal limits. They used an instantaneous derating strategy with varying temperature reduction gradients. Though they were able to achieve their goal of safely operating close to the thermal limits, the issue of torque oscillation which results in drivetrain oscillations caused by the temperature based derating was not addressed.

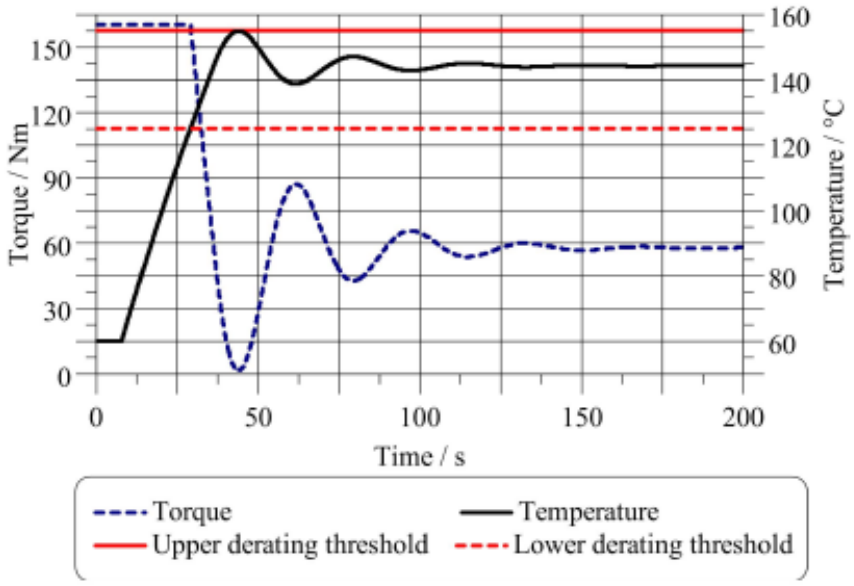

Figure 1: Electrical drive temperature and torque response during thermal derating *[40]*

Drivetrain oscillations are very common in electric vehicles because they are usually not equipped with dampers since the torque produced by the traction drive is linear [42]. Drive train oscillations could be as a result of sudden load change [3] [40] operating in certain regions, such as field weakening [43], oscillation in voltage as a result of resolver error [44], during regenerative braking [45] etc. Conventional combustion engine driven vehicles on the other hand are usually equipped with dampers because of the non-linear torque produced by the combustion engine. Most studies in drivetrain oscillations in both conventional and electric vehicles are based on oscillations resulting from gear switch, driving on an uneven surface or abrupt change driving torque request [42] [46] [47]. This approach usually aims to compensate for the mechanical resonance of the system.

An abrupt change in the driver request torque when approaching the thermal limit can lead to drivetrain oscillations as shown in Figure 1. The conventional approach to solving such oscillations will be to compensate for the mechanical resonance. For thermal based oscillations, this is a risky proposition because to compensate for the mechanical resonance, a torque of the same oscillating frequency in opposition to the oscillating driving request torque has to be generated. There is a risk that this additional torque could result in operation over the thermal limit or if it is limited together with the driving request torque, might not be sufficient to compensate for the resulting oscillation. A better alternative to resolve such thermal based oscillations will be to implement a derating strategy which allows for safe operation close to the thermal

limit without abruptly reducing the torque. Predictive derating strategies prevent unwanted drivetrain oscillations [41] and also provide useful information about future maximum allowed torque/current which is relevant for optimal operation of the vehicle [41] [48].

In order to optimally operate an electric drive close to its thermal limit, accurate information about the inverter junction temperature is required. During operation of electric drives, the inverter temperature changes faster than the electric machine temperature because the inverters have a lower thermal time constant than the electric machines. Determining the correct thermal impedance of the inverter is critical in accurately estimating the junction temperature. In [49] we presented a method for determining thermal impedances from VCE based TSEP and direct temperature measurement. We validated this method using measurements from an infrared camera. The results presented in [49] are based on a 3rd order thermal impedance network model.

In [50], we used the same experimental setup, but a novel method for extracting the thermal impedance parameters using the well-known least squares method was presented. This method takes advantage of the availability of development IGBT module with temperature sensors within close proximity to the transistor and diodes. These modules are used primarily in the validation of calculated junction temperatures. The novel least squares based approach eliminates the sources of error from the TSEP based VCE methods which rely heavily on the accuracy of the measured voltages across the transistors and diodes as well as those measured temperatures in the cool down phase.

The results of the junction temperature calculated using the novel method presented in [50], are compared to those obtained from TSEP VCE based approach presented in [49]. This method is an analytical method and well suited for implementation on a microcontroller. However, due to the limited computational power of microcontrollers used for mass production purposes, it is imperative to study the effect of the order of the thermal impedance network on the accuracy of the calculated junction temperature to obtain the optimal compromise between computational recourses and accuracy of the calculated junction temperature. The method we presented in [50] is the key scientific contribution of this theses.

1.3. Thesis Objectives

The aim of this thesis is to implement an optimal thermal management strategy for an electric traction drive allowing maximum possible torque for the given operating condition while guaranteeing thermal safety of the drive system. A detailed analytical thermal model for the inverter to accurately estimate the junction temperature is established by accurate characterization of the thermal impedance network. Based on the

estimated temperature and other important parameters, a derating strategy for optimum performance has to be implemented. Since most state of the art thermal models rely on a fixed parameter set measured under a defined operating condition, estimation of junction temperature under changing environmental and operating conditions might be inaccurate. Hence a method for online adaptation of thermal model parameters to changing environmental and operating conditions will be investigated in later stages of the thesis.

2. Inverter Power Loss and Thermal Impedance Network

Junction temperature depicts the maximum temperature of a semiconductor in operation. This is a virtual temperature usually calculated from a reference temperature using the power loss in the semiconductor and the thermal network which describes the temperature difference between the reference temperature and the junction temperature for the given operating condition. The reference temperature is usually referred to as the heat sink temperature while the junction temperature is referred to as the heat source temperature. The temperature difference between the heat source and the heat sink is determined by the product of the power loss generated by the heat source and the thermal impedance between the heat source and the heat sink. Since the heat sink temperature is usually known (measured), an accurate estimation of the junction temperature will greatly depend on the quality of the thermal impedance network between the heat source and the heat sink as well as the accuracy of the estimated power loss throughout the entire operating range of the inverter.

Inverter power loss resulting from the resistance to the flow of current through the power modules is known as the conduction loss. The operation of the inverter involves the transistors switching ON and OFF at usually very high frequencies. These ON/OFF switching of the transistors result in additional power loss known as switching losses. Thermal impedance on the other hand represents the heat transfer path between the heat source and the heat sink. The thermal impedance between the heat source and the heat sink is usually represented by an RC network consisting of thermal resistance and capacitances. The thermal impedances represent the quantity of heat transferred between the heat source and the heat sink while the thermal capacitance represents the thermal time constant (rate of heat transfer between heat source and heat sink). Inverter power loss and thermal impedances are discussed in details in the subsequent chapters.

2.1. Inverter Power Loss

Inverter power loss consists of switching losses and conduction losses. Switching losses result from energy loss during turn on and turn off the inverter switching elements while the inverter is in operation. Conduction losses on the other hand are resistive losses caused by current flow through the switching elements.

2.1.1. Switching Loss

Inverter switching losses consists of IGBT turn-on and turn-off power losses as well as the diode reverse recovery energy loss. The switching losses greatly depend on the gate resistance or commutation current of the IGBT, the DC-link voltage, the collector emitter current or diode forward current and the junction temperature of the IGBT or diode [51] [52] [53] [54]. IGBT turn-on and diode turn-off characteristics for a 150A/1700V IGBT [53] is shown in Figure 2 below.

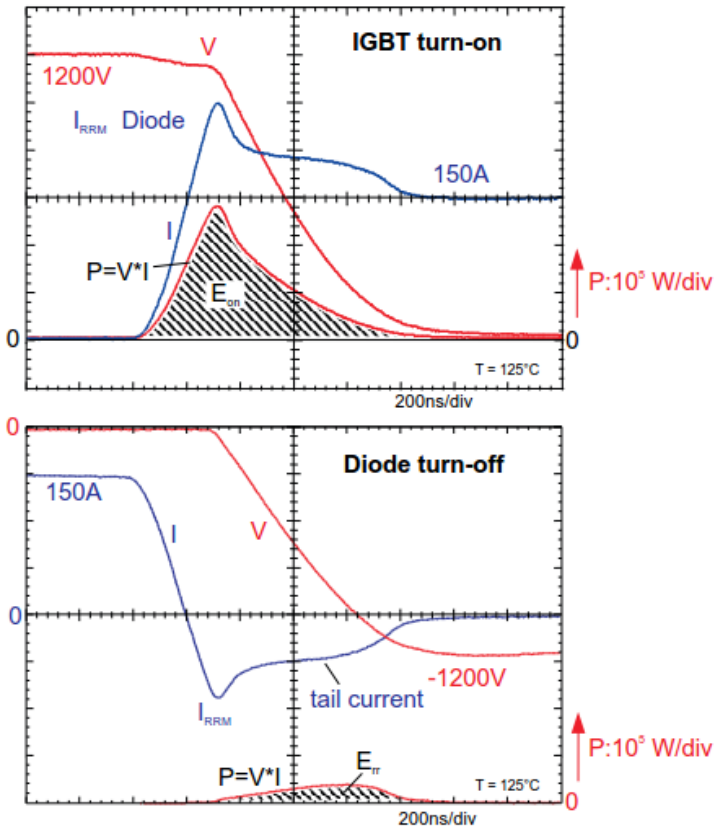

Figure 2: Current, voltage and power losses during turn on of a 150 A / 1700 V IGBT and diode Turn-off during recovery behaviour measurements *[53]*

IGBT turn-on and turn-off energies and the diode reverse recovery energy are can be extracted from turn on and turn-off characteristics curves from the IGBTs and diodes as described in [51] [52] [54].

2.1.2. Conduction Loss

IGBT and diode conduction loss parameters V_{ce0} (IGBT saturation voltage), V_{F0} (diode forward voltage), R_s (collector-emitter resistance), R_f (diode forward resistance) are determined from the IGBT transfer characteristics Figure 3 and the forward diode characteristics Figure 4.

A suitable operating temperature for which the conduction loss parameters are to be determine is chosen. A straight line is drawn on the V_{CE} or V_F characteristics in the linear region (usually in the high current voltage region). The intersection of the straight line on the V_{CE} or V_F axis (zero current) is the desired V_{CE0} or V_{F0}. R_S or R_F are computed from the inverted gradient of the straight line as shown in Figure 3 and Figure 4.

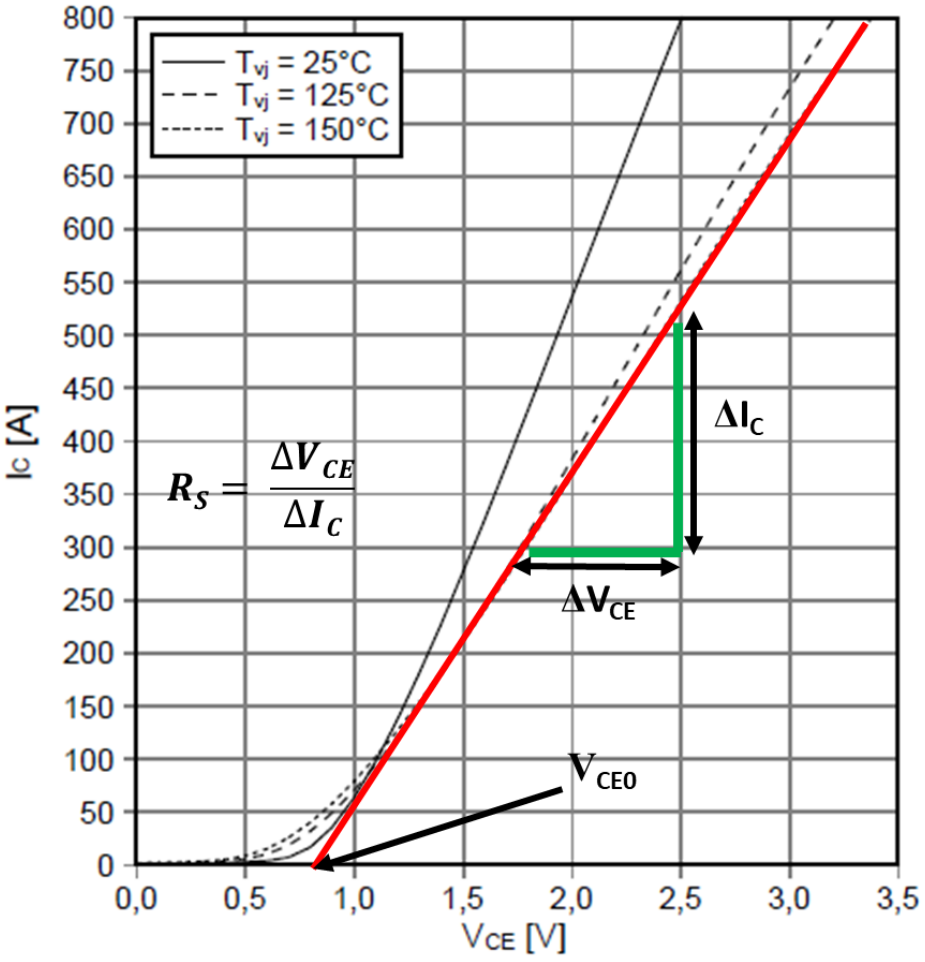

Figure 3: IGBT transfer characteristics [20]

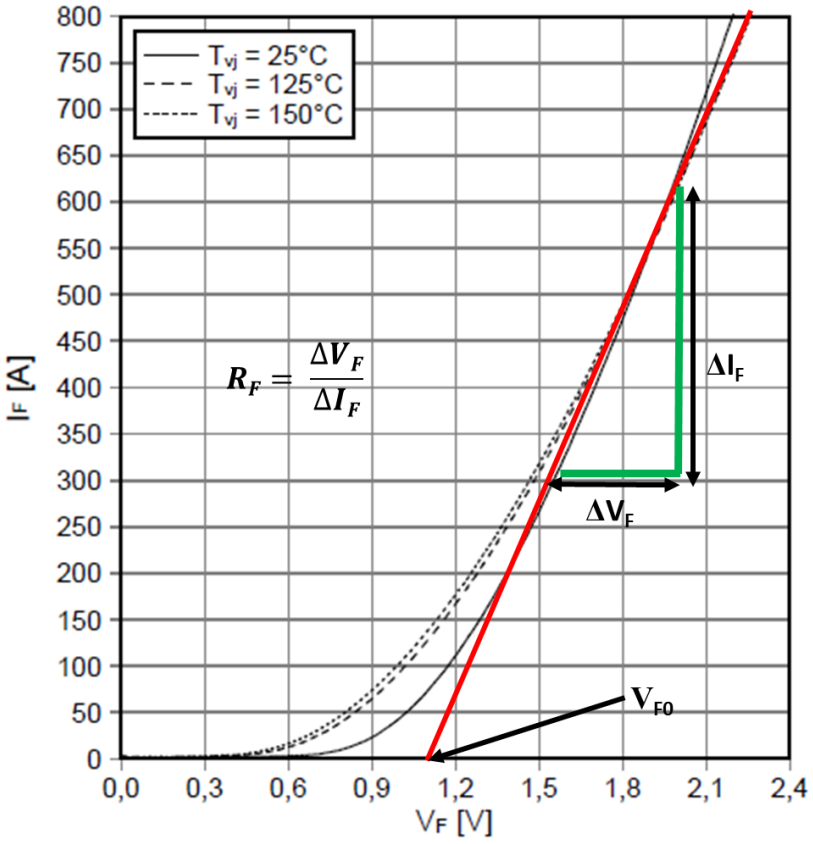

Figure 4: Diode forward characteristics [20]

IGBT and diode power loss (P_T and P_D respectively) consist of conduction and switching losses calculated according to [55] [53] as follows:

$$\boldsymbol{P_{T(i)} = P_{con,T(i)} + P_{Switch,T(i)}} \quad 2.1$$

$$\boldsymbol{P_{D(i)} = P_{con,D(i)} + P_{Switch,D(i)}} \quad 2.2$$

$$\boldsymbol{P_{con,T(i)} = (I_{T(i)} * V_{ce0} + I^2_{T(i)} * R_s) * a_{T(i)}} \quad 2.3$$

$$\boldsymbol{P_{switch,T(i)} = \frac{(E_{on} + E_{off}) * F_{switch} * I_{T(i)} * V_{dc}}{I_{Nom} * V_{Nom}}} \quad 2.4$$

$$\boldsymbol{P_{Con,D(i)} = (I_{D(i)} * V_{F0} + I^2_{D(i)} * R_f) * a_{D(i)}} \quad 2.5$$

$$P_{switch,D(i)} = \frac{E_{rec} * F_{switch} * \sqrt{I_{D(i)}} * V_{dc}}{\sqrt{I_{Nom}} * V_{Nom}} \quad 2.6$$

where $a_{D(i)}$, $a_{T(i)}$ = duty cycle of ith diode or IGBT, F_{switch} = switching frequency, $I_{T(i)}$, $I_{D(i)}$ = current through ith IGBT, diode.

Parameters V_{ce0} (IGBT saturation voltage), V_{F0} (diode forward voltage), R_s (collector-emitter resistance), R_f (diode forward resistance), E_{rec} (diode recovery energy), E_{on} (IGBT turn on energy), E_{off} (IGBT off energy), I_{Nom} and V_{Nom} are obtained from the datasheet [19]. Look-up tables are implemented to consider the variation of parameters V_{ce0}, V_{F0}, R_s, R_f, E_{rec}, E_{on} and E_{off}, with temperature. I_{Nom} and V_{Nom} are currents and voltages at which the parameter measurements are done.

2.2. Thermal Impedance Network

The temperature difference between the junction and ambient temperature can be represented by the product of the power loss P causing junction temperature increase and the equivalent thermal impedance Z_{th} between the junction temperature T_{jnc} and the ambient temperature T_{amb} [37] [56] [57] [58].

$$Z_{th} = \frac{T_{jnc} - T_{amb}}{P} \quad 2.7$$

Thermal impedance network can be represented as an analytical R-C network [28] comparable to that of electrical circuits. The thermal impedance is the equivalent thermal resistances and thermal capacitances between the ambient temperature and the junction temperature. The thermal impedance network can be represented in many different ways, depending on the objective of the thermal model and the amount of information at hand. The two most widely used R-C network types in thermal impedance modelling of IGBT modules are the Foster (partial fraction circuit) and Cauer (continued fraction circuit) networks.

2.2.1. Cauer Network

The Cauer network Figure 5 also known as the grounded capacitor network [59] [60]has the main advantage that it is derived from the fundamentals of heat transfer and represents a meaningful physical representation of the transfer path in the system [59] [60] [61].

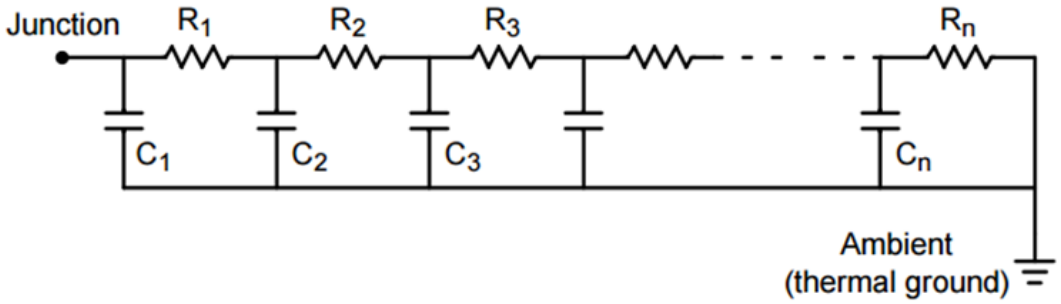

Figure 5: Cauer network *[59]*

Each node in the network can be associated with a defined heat transfer path of the IGBT module, for example IGBT Module → Thermal grease → Heat Sink → Ambient as shown in Figure 6.

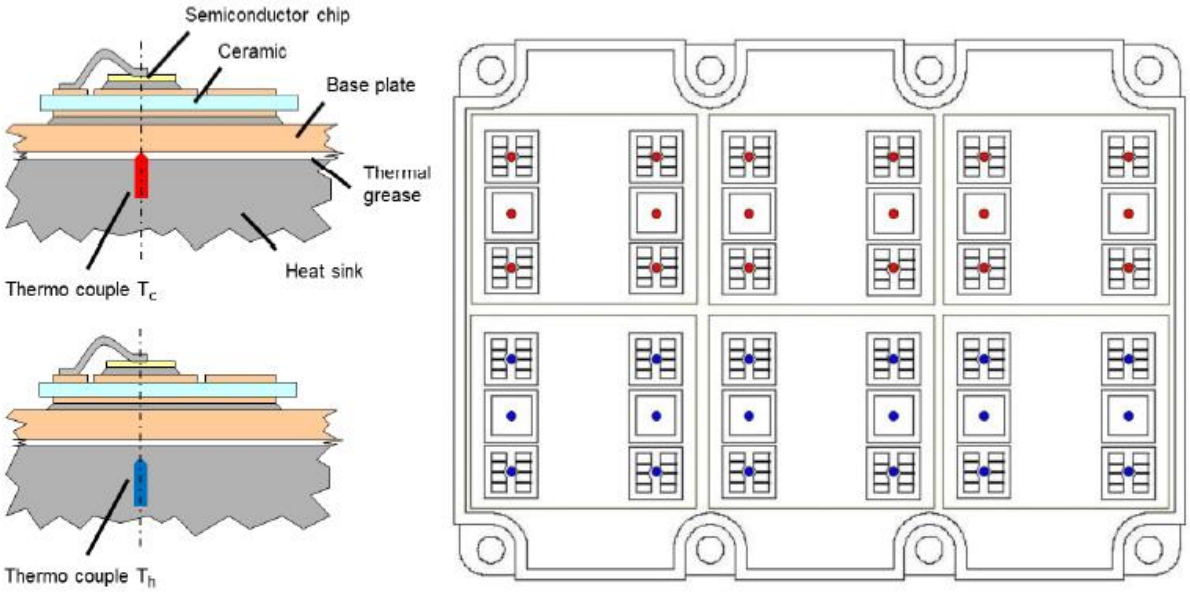

Figure 6: Determination of case temperature T_c and heat-sink temperature T_h and example for the projected sensor positions based on a 3.3 kV 140x190 mm^2 module *[60]*

The Cauer network for the IGBT module shown in Figure 6 is shown in Figure 7. An accurate thermal model in this case will require determination of the heat sink temperature, the thermal grease temperature and the junction temperature based on the separate thermal impedances between each node as shown in Figure 7.

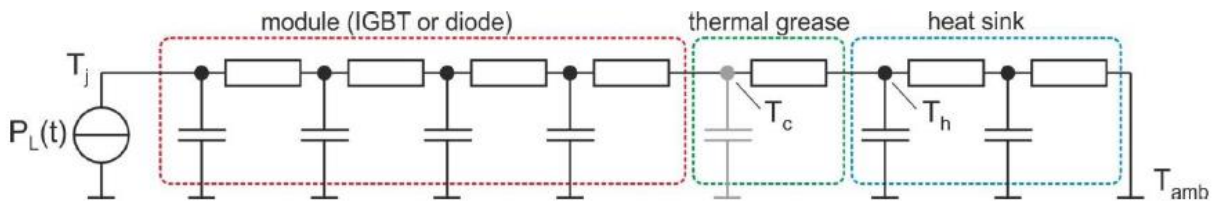

Figure 7: Merging continued-fraction models to a system model *[60]*

Though Cauer networks provide a detail representation of the heat flow path in the module, the mathematical representation is complicated [60] [61] and accurate determination of the parameters could prove challenging.

2.2.2. Foster Network

Foster network of Figure 8 also known as the non-grounded capacitor network [59] is a simple representation of the heat transfer path between two points with no direct physical meaning [59] [61].

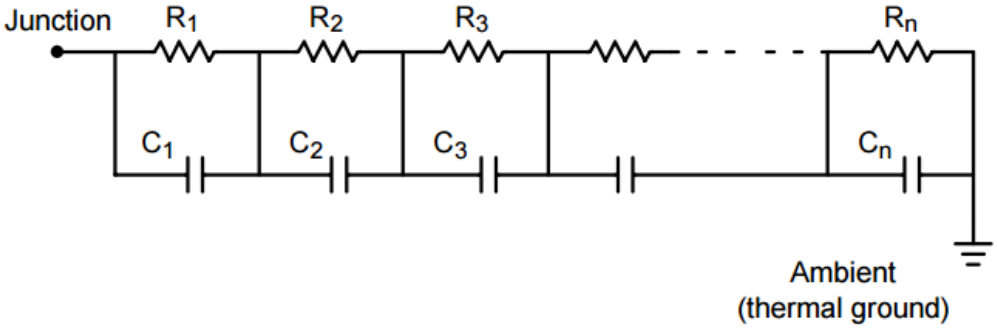

Figure 8: Foster network *[59]*

The Foster network for the IGBT module shown in Figure 6 is shown in Figure 9. An accurate thermal model in this case will not require determination of the heat sink temperature, the thermal grease temperature and the junction temperature based on the separate thermal impedances between each node as shown in Figure 9. Only the thermal impedance network between the junction and the ambient temperature is required in this case.

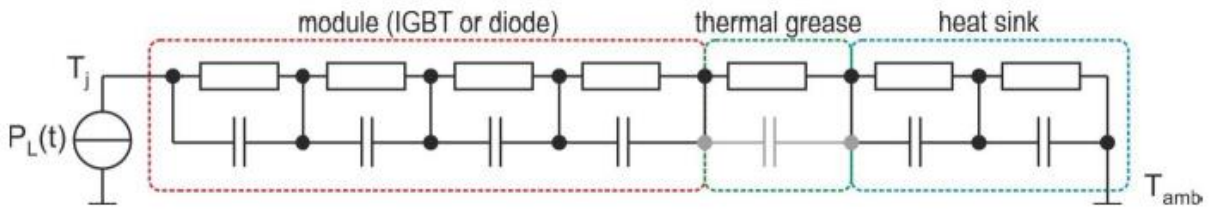

Figure 9: Merging partial-fraction models to a system model *[60]*

The mathematical representation of the Foster network is not complicated, the parameters are easy to determine. Cauer networks can be converted to Foster network to produce a similar step response thermal step response [61]. In this case, the end temperature will be approximately the same, but the dynamics of the temperature rise might slightly differ if there are some differences between the thermal impedance networks of the individual nodes of the Cauer network.

The exact determination of thermal impedance between the different nodes of a Cauer network sometimes involves the use of finite element methods to model the IGBT module [60]. This is also challenging because a detailed information about the material property of each layer is required. In this thesis, the focus is on determining the Foster thermal impedance network of an IGBT module based on experimental measurements. These measurements are based on the state of the art methods for determining the Thermos-Sensitive Electrical Parameters (TSEP).

2.2.3. Thermo-Sensitive Electrical Parameters

The most widely used industrial method for determining junction temperature for power modules is the use of thermo-sensitive electrical parameters (TSEP) [62] [63] [64] [65]. TSEPS depict the physics of the relationship between the electrical parameters of the power module and its junction temperature. This is usually derived from the measurement of an electrical parameter of a power module as a function of the junction temperature [29] [66] [67]. In the case of IGBT modules, the transistor collector-emitter voltage and the diode forward voltage are usually measured. Several different principles can be applied in the determination of TSEPs. These principles are discussed in the next sections.

2.2.3.1. Classical (Offline) TSEPs

Offline TSEPs are used in the determination of the thermal impedance network (thermal resistance and capacitances) [62]. They are also very suitable in modelling aging behaviour of power modules. Most widely measure parameters using this method in-case of IGBT modules are transistor collector-emitter voltage or diode forward voltage at very low current. Offline TSEPs are usually measured in a single

(usually open) non-functional IGBT module. Offline TSEPs have a very high accuracy but the main drawback is that the power module will have to be modified for it to be used in a functional system (inverter).

2.2.3.2. Static characteristic I (V) TSEP

This method involves simultaneous measurement of a voltage and current crossing a device [62] [68] [69]. The main advantage of this method is that it can be applied to a functioning system (inverter) without major alteration if the sensors required in control of the inverter can be used. A major disadvantage of this method is that very high accuracy sensors are required which would increase the overall cost of the system. There are also resistances in the module which might cause the measurements to be inaccurate during operation.

2.2.3.3. Dynamic Characteristics

The dynamic characteristics such as turn-on delay, turnoff delay, or rate of change of current during turn-on can also be used in determining junction temperature [62] [68]. Though dynamic TSPEPs can be applied to a functional system, the major disadvantages of dynamic TSEPs is that it can only be applied to switching elements (transistors) as well as their low sensitivity. During operation dynamic TSEPs also present a challenge in that they are very sensitive to switching speeds of transistors, the voltage, current, gate resistance and gate–emitter voltage.

3. Determination of Thermal Impedance Network from Direct Temperature Measurement

The determination of thermal impedance network in this thesis is based on classical TSEPs because of their high accuracy. The idea is to characterize the thermal impedance network offline. Since knowledge of the power loss of the IGBT module is known, the characterized thermal impedance network can be used in estimating the junction temperature during operation.

3.1. Experimental Setup

The experimental setup for thermal impedance measurement as reported in [70] is shown in Figure 10

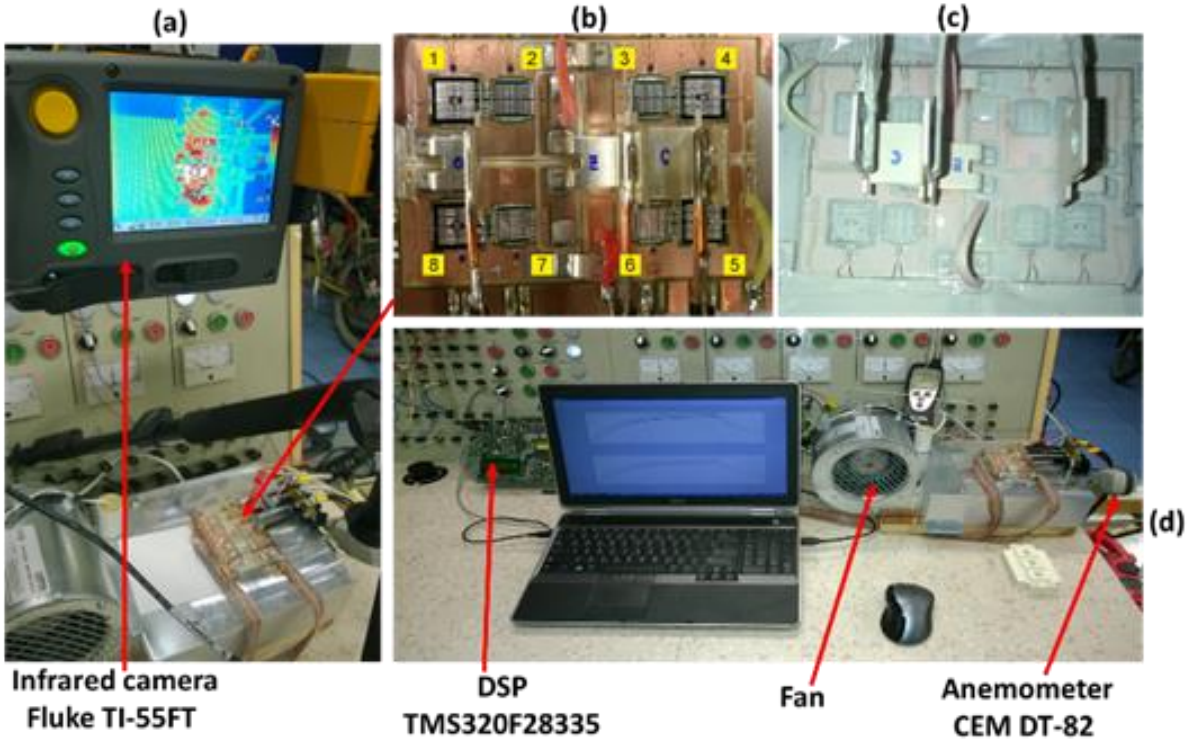

Figure 10: Experimental setup for Zth measurement *[70]*

The device under test is a half-bridge IGBT module with two parallel connected IGBTs and two parallel connected diodes the top and bottom sections. An opened IGBT module with isolating gel washed out as shown in Figure 11 is used in this experiment. It is important to wash away the isolating gel so that temperatures as closed to the junction temperature as possible can be measured in steady state. During this

experiment, the IGBT module is not operated in a switching state and the maximum allowed current is also greatly limited. The maximum current is used in the measurements is 50A.

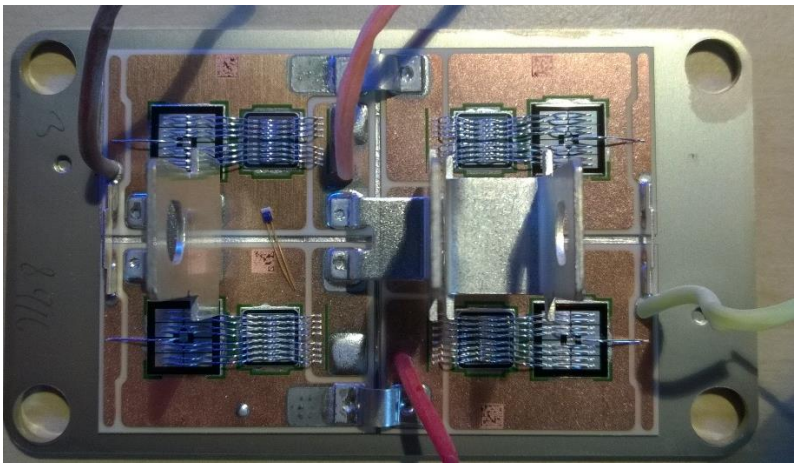

Figure 11: Opened IGBT module with isolation gel washed out

In order to measure IGBT and diode steady state temperatures as closed to the junction as possible, Pt100 temperature sensors numbered 1 – 8 in Figure 10 (b) and Figure 12 are placed closed to the IGBT and diodes. Theses sensors are used for validation of the thermal model developed using from the classical TSEP based thermal impedance network.

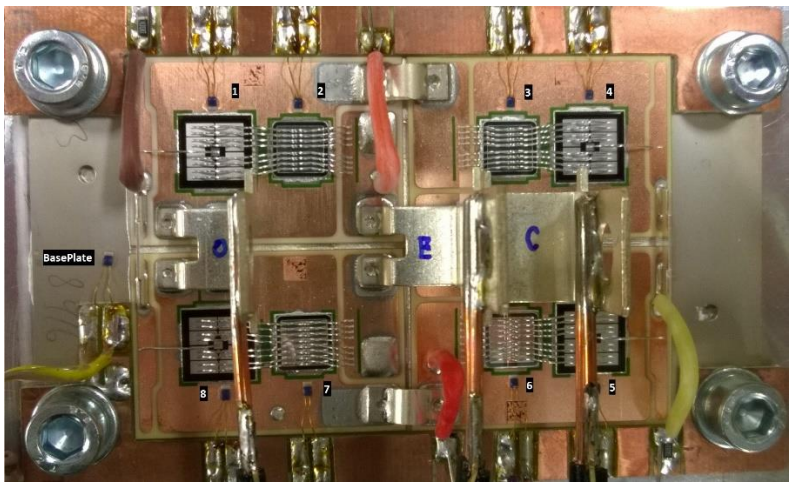

Figure 12: Location of pt100 sensors in opened IGBT module

The IGBT module mounted on an aluminium heat sink is attached to a cooling fan as shown in Figure 10 (d) and Figure 13. The cooling fan is operated as suitable speeds to obtain the required air flowrates for determining the thermal impedance. This is important because the variation of the thermal impedance under different cooling conditions is studied in these theses. Selected air flowrates for this study are 0m/s, 0.5m/s, 5m/s, 14m/s. An anemometer as shown in Figure 10 (d) and Figure 14 is used in measuring the air flowrate.

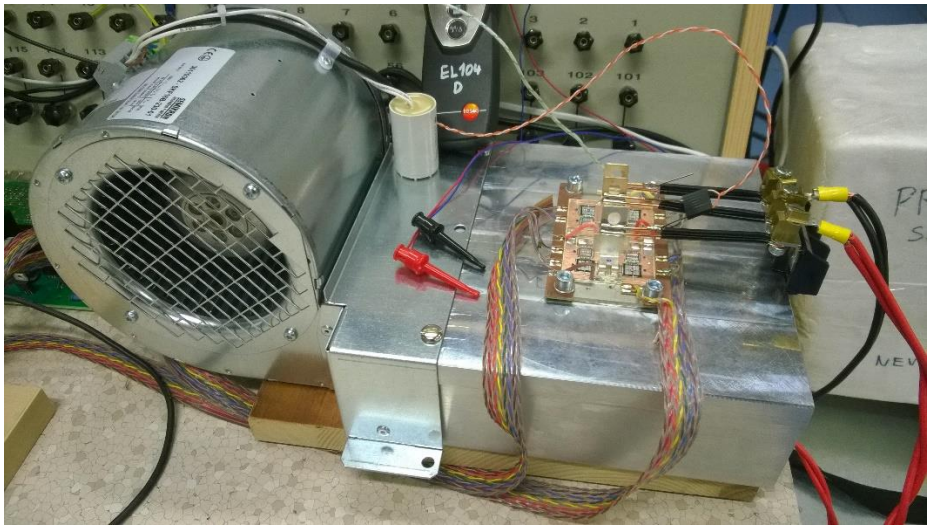

Figure 13: IGBT module mounted on cooling fan

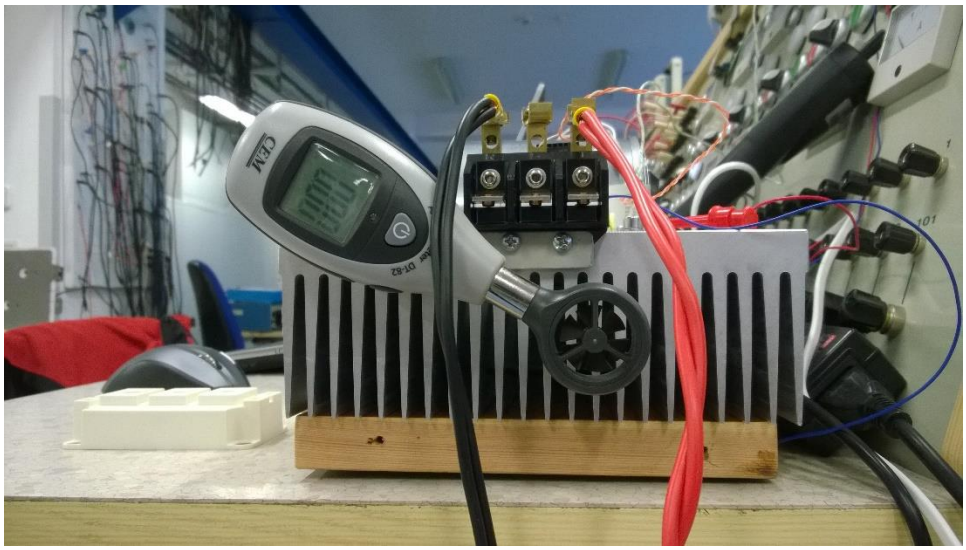

Figure 14: Anemometer used in measuring airflow rate

An infrared camera as shown in Figure 10(a) and Figure 15 is used in measuring the steady-state transistor and diode temperatures. This is also used in the validating of the thermal model. The infrared camera is located above the IGBT module mounted on the cooling fan at a suitable distance to optimally capture the transistor and diode temperatures.

In order to enhance the quality of the infrared images, a thermal spray is applied to the open IGBT module as shown in Figure 10(c) and Figure 16. The emissivity of the thermal spray has to be suitably selected so that the thermal characteristics of the diode or transistors are not altered which could lead to a wrongly determined thermal impedance. The emissivity of the spray used in this experiment is 0.97.

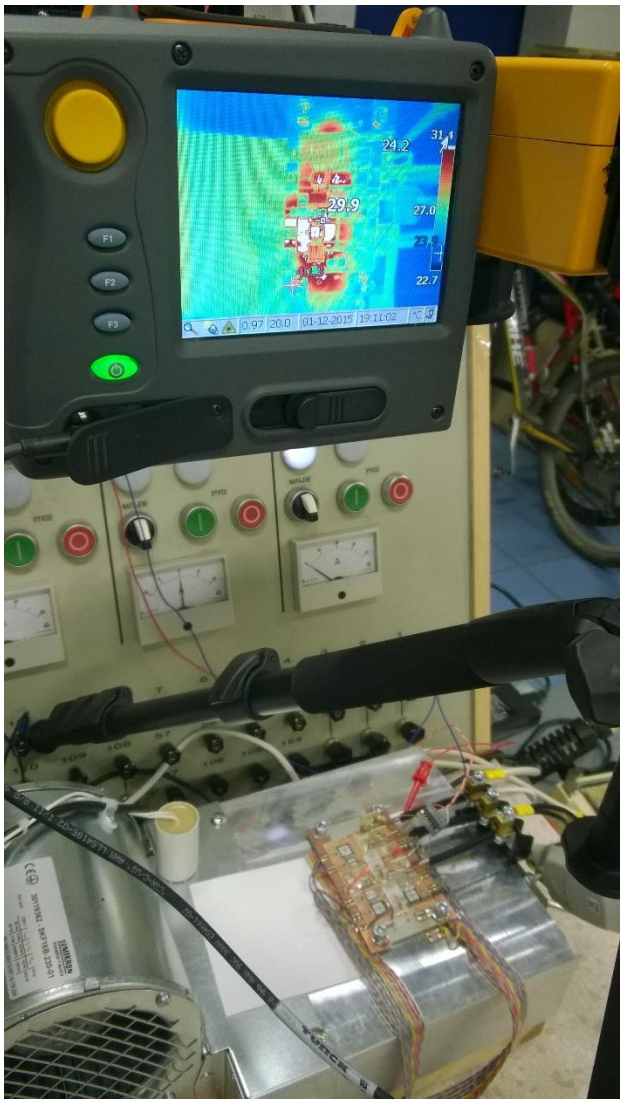

Figure 15: Infrared camera for measuring transistor and diode temperatures

Figure 16: Opened IGBT module sprayed with thermal spray

Currents, voltages and temperatures are measured by the DSP in in Figure 10(d) and transferred via USB to the laptop where they are stored in MAT file format.

3.2. Measurement of Current, Voltages and Temperature

Measurement of currents, voltages and temperatures required for determination of thermal impedance is done using the circuit of Figure 17. The experiment is conducted at room temperature.

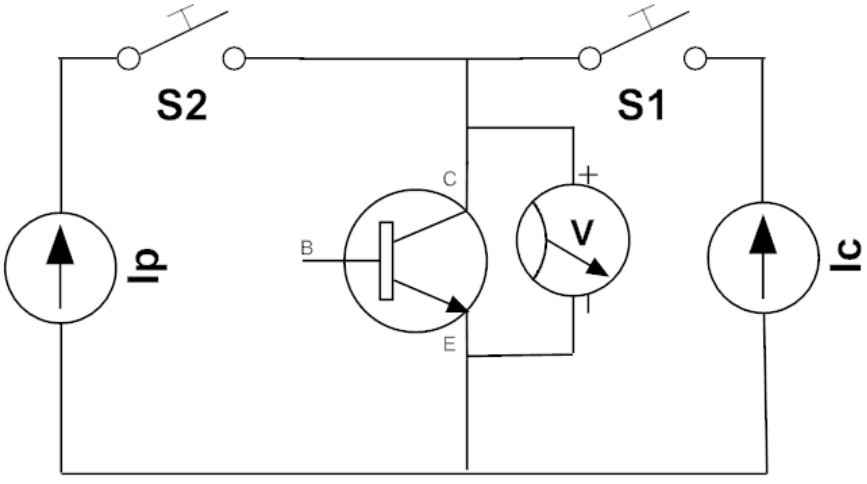

Figure 17: Circuit used in direct and voltage-based temperature measurement [70]

The switch S1 is closed throughout the experiment. This allows small amount of calibration current which does not account for any temperature increase in the IGBT or diode during the experiment to flow through the IGBT or diode so that that the switching element remains active through the entire measurement. Switch S2 is closed so that a current (e.g. 50 A) flows and heats up the IGBT or diode until steady state temperatures are measured as shown in Figure 18. After steady state is attained for a defined period of time, switch S2 is open to allow the device under test to cool down at the defined coolant air flowrate. The temperatures of all switching elements, the current through the circuit and the voltage of the IGBT or diode under test are measured as shown in Figure 18.

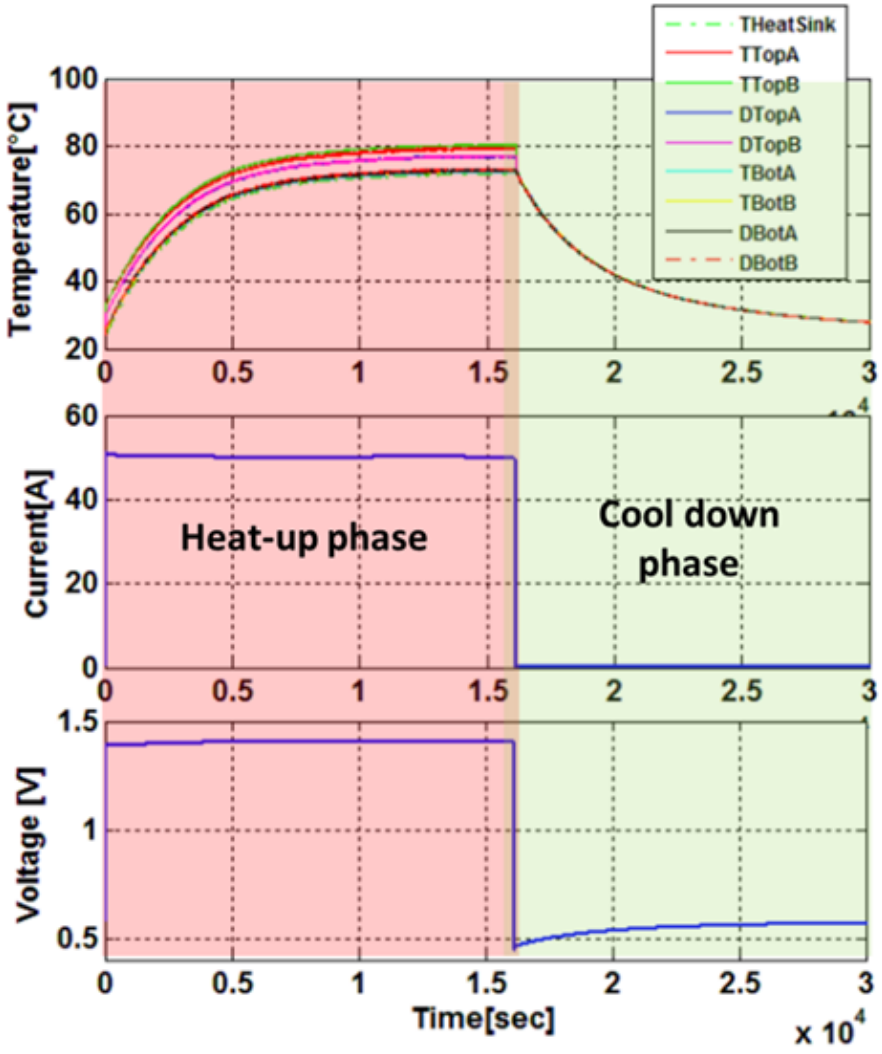

Figure 18: Temperature, current and voltage profiles during measurement

A linear relation between, measured voltage and temperature is expected to correctly characterize the thermal impedance network. If the calibration current is too small, the relationship between measured voltage and junction temperature will be non-linear [36] . For this experiment, a calibration current of 100mA is deemed suitable.

Experimental data is collected for the following operating conditions indicated in Table 1.

Table 1: Experimental data collection operating conditions

Currents [A]	**Air flowrate [meters per second m/s]**				
25	0	0.5	1	5	14
50	0	0.5	1	5	14

Each element of the IGBT module (top diode, top transistor, bottom diode, bottom transistor) is operated individually under the conditions defined in Table 1 and its corresponding set of experimental data is recorded. These operating conditions are chosen to test the performance of the proposed model under different cooling conditions. Designation of the experimental data starts with the active element, followed by the air flowrate and the current. For example Ttop_1mps25A is data collected for an active top transistor at current of 25A and 1 meters per second cooling air flowrate.

3.3. Calibration Curve

The calibration curve depicts the relationship between voltage drop across IGBT or diode and junction temperature. The measurement procedure described in 3.2 above at 0m/s airflow rate is used in the calibration curve. The temperatures and voltage drop across IGBT or diode during homogenous cool down at 0m/s the same temperature is measured on IGBT, diode and heat sink are recorded and used in the determination of the relationship between voltage drop across IGBT or diode and junction temperature. The IGBT and diode calibration curves for this experiment are as shown in Figure 19 and Figure 20.

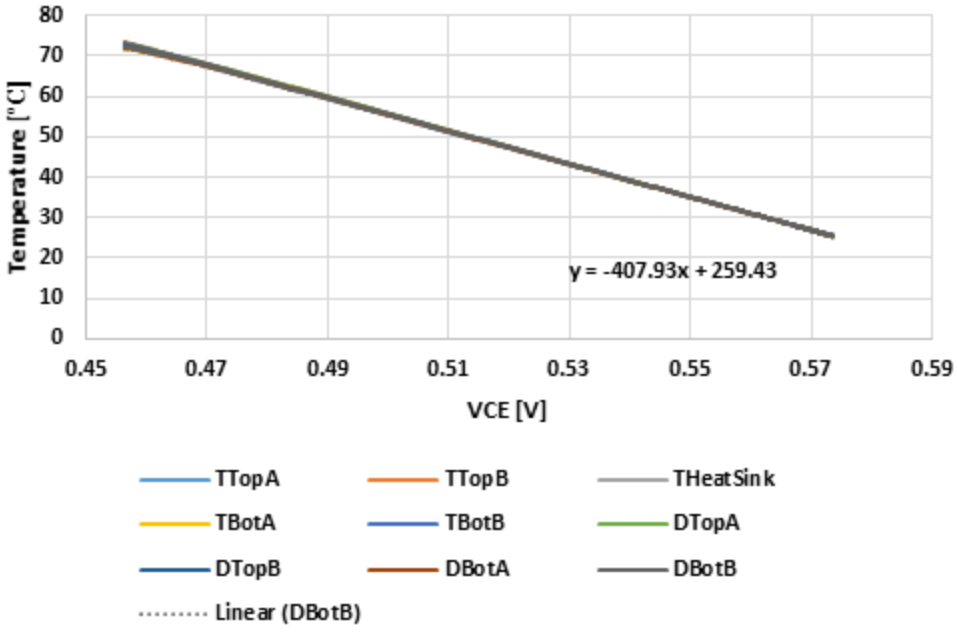

Figure 19: Calibration curve IGBT

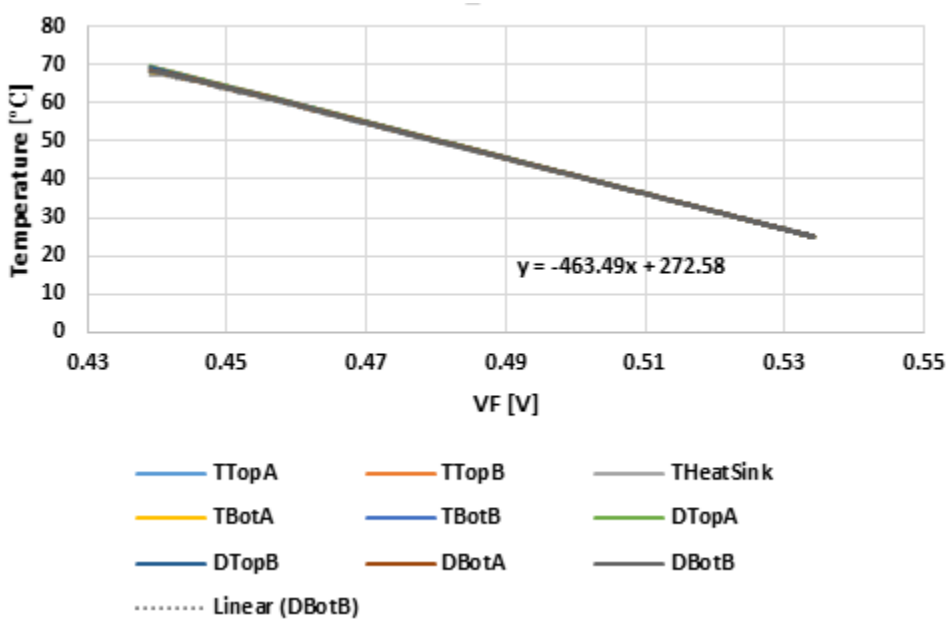

Figure 20: Calibration curve diode

Linear relationship between junction temperature and voltage drop across IGBT and diode from Figure 19 and Figure 20 are established as follows:

$$T_{Jnc_{IGBT}} = -407.93 * VCE + 259.43 \quad 3.1$$

$$T_{Jnc_{diode}} = -463.49 * VF + 272.58 \quad 3.2$$

Linear equations 2.8 and 2.9 depicting the relationship between voltage drop across IGBT or diode and their respective junction temperatures are used in calculation of junction temperatures of the respective IGBT or diode during the cool down phase. This information is required in the determination of the Foster network parameters explained in section 3.4.

3.4. Foster Network Parameter Extraction

Foster network parameters for the active elements are determined from voltage drop across IGBT or diode and measured temperature in the cool down phase. The measured voltage-based IGBT or diode junction temperature is calculated using the voltage-junction temperature equation established from the calibration curve and the measured voltage drop across the IGBT or diode.

Voltage and temperature profiles used in determining Foster network parameters at 5m/s air flowrate is as shown in Figure 21 and Figure 22.

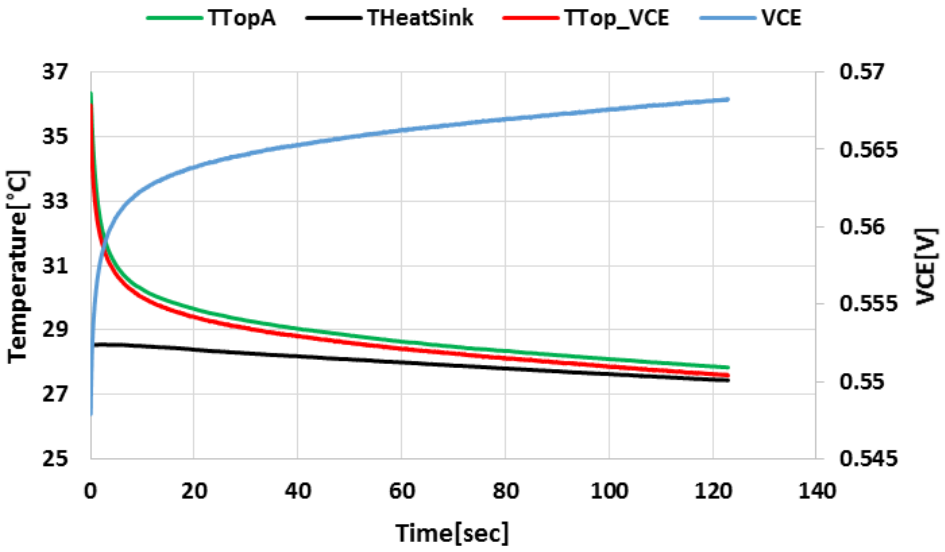

Figure 21: VCE and temperature profiles of IGBT in cool down phase at 5m/s air flowrate

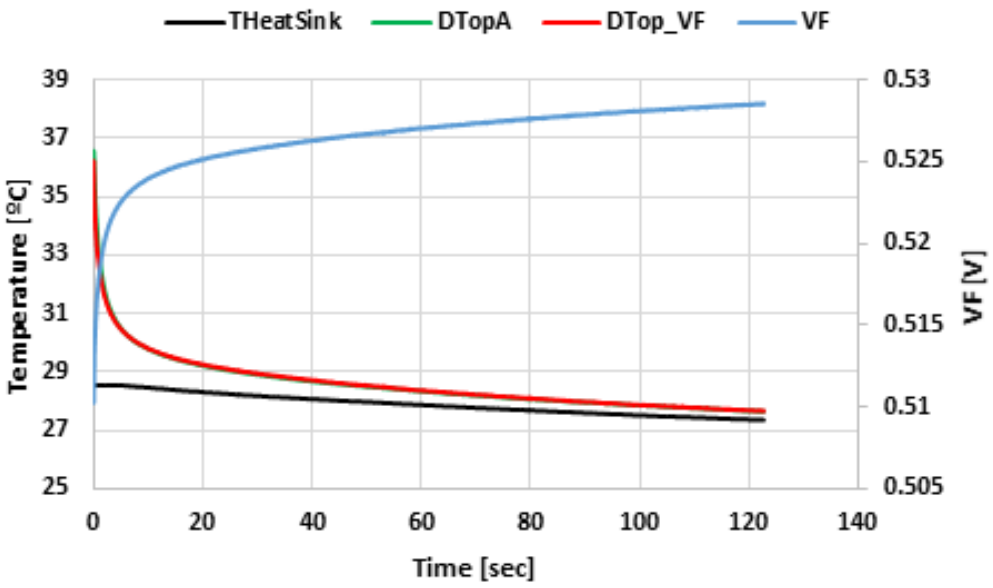

Figure 22: VF and temperature profiles of diode in cool down phase at 5m/s air flowrate

TTopA, DTopA and THeatSink are measured top IGBT, top diode and heat sink temperatures respectively. TTop_VCE and DTop_VF are top IGBT and top diode temperatures calculated from the measured collector emitter voltage VCE and forward voltage drop across diode VF, using the calibration curve equations 2.8 and 2.9.

The thermal impedance Zth is calculated from equation 2.7 where T_{Jnc} is the IGBT or diode junction temperature measured or voltage-based, P is the IGBT or diode steady state power loss, T_{amb} is the measured heat sink temperature THeatSink.

From the data obtained using equation 2.10 the Foster network parameters are determined using curve fitting technique. The general equation used in the Foster network parameter extraction for the active and passive switching elements is as follows:

$$\boldsymbol{Zth(t)} = \sum_{\boldsymbol{i=1}}^{\boldsymbol{3}} \left[\boldsymbol{Ri} \times \left(\mathbf{1} - \boldsymbol{e}^{\frac{-t}{Ri \times Ci}}\right)\right] \qquad 3.3$$

Ri is a representation of steady state thermal impedance while *Ci* is a representation of the dynamic behaviour (heat transfer coefficient). Three first order systems are used because it was observed that increasing the number of first order systems does not necessarily improve the accuracy of the fit. Higher

number of first order systems may also prove problematic if the thermal network is to be implemented on a microcontroller with limited computation capacity.

IGBT and diode Zth curves of measured and fitted data at 5m/s coolant flowrate are shown in Figure 23 and Figure 24.

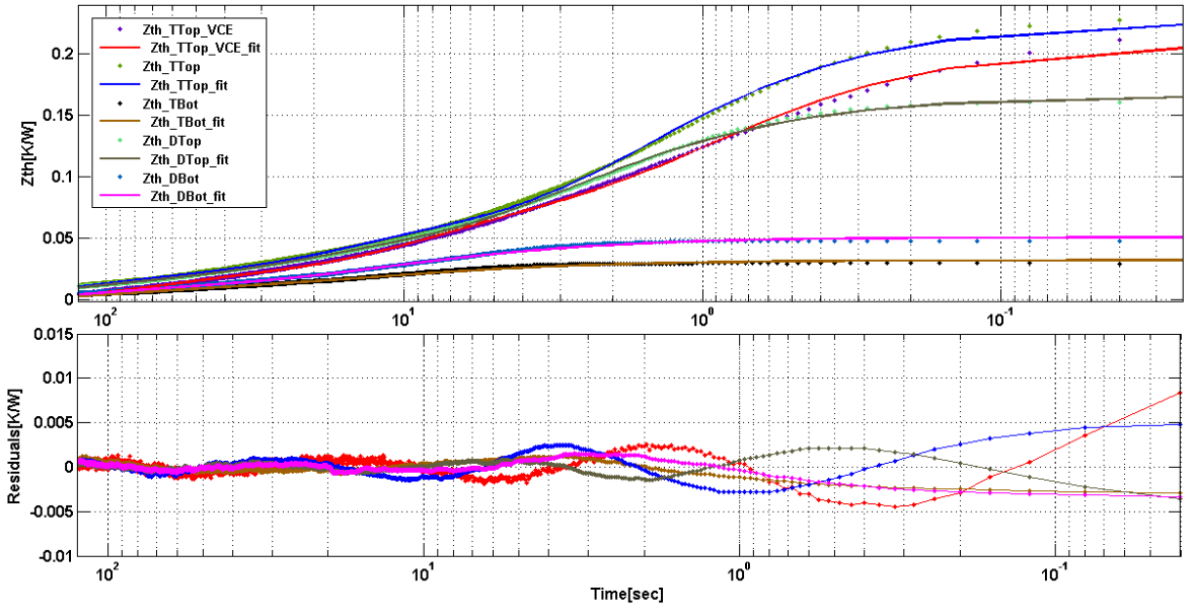

Figure 23: Zth curves for active top IGBT at 5m/s air flowrate

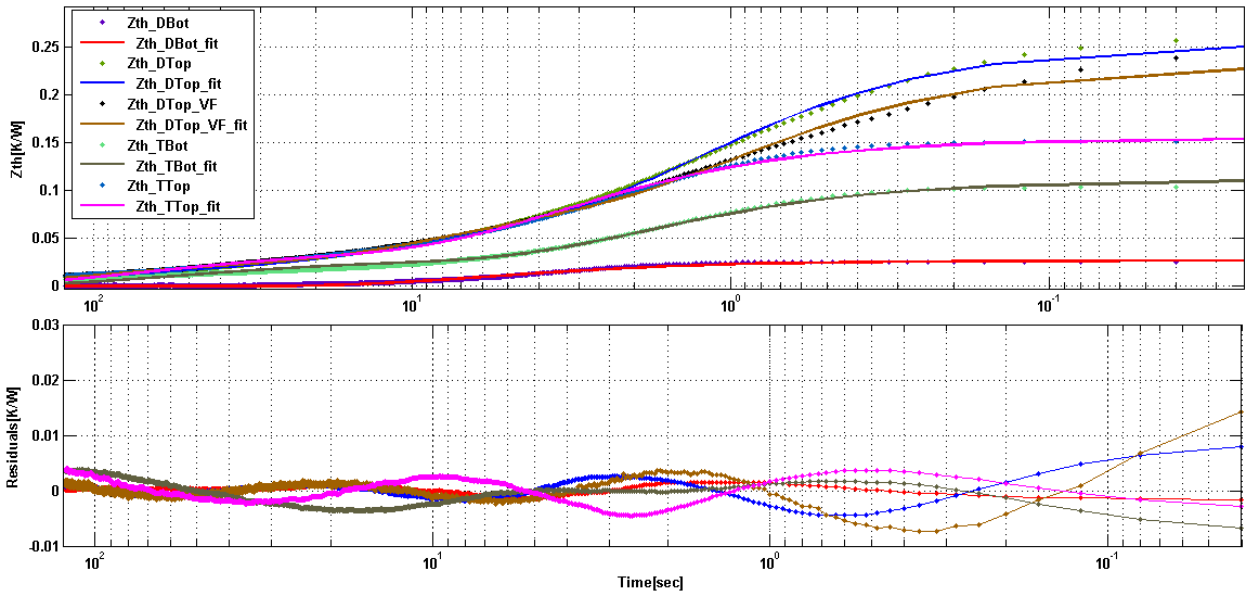

Figure 24: Zth curves for active top diode at 5m/s air flowrate

Zth_TTop_VCE is the thermal impedance of the active top IGBT calculated from voltage-based temperature method, Zth_TTop, Zth_TBot, Zth_DTop, Zth_DBot are thermal impedances of top and bottom IGBTs and diodes. The _fit are the respective fitted curves.

The residuals (difference between data and fitted curve) are between -0.005 and 0.01 showing that equation 2.10 provides a good fit to the measured data.

The logarithmic scale is used because it provides a better representation of the dynamic behaviour. Due to the fact that the thermal impedance is determined from the cool down phase, the time axis is reversed.

The Ri and Ci parameters of equation 2.10 obtained from Figure 23 and Figure 24 are shown in Table 2 and Table 3 respectively.

Table 2: Zth parameters for active top IGBT at 5m/s air flowrate

	TTop_VCE	TTop	TBot	DTop	DBot
R1[K/W]	0.07221	0.05618	0.01422	0.09383	0.02112
R2[K/W]	0.09852	0.03386	7.15E-07	0.02942	0.01349
R3[K/W]	0.03778	0.1366	0.0185	0.04315	0.01671
C1[Wsec/K]	81.74	193.4	622	23.99	4000
C2[Wsec/K]	7.62	3264	5.534	3999	694.9
C3[Wsec/K]	1524	9.948	3999	322	568.1

Table 3: Zth parameters for active top diode at 5m/s air flowrate

	TTop	TBot	DTop_VF	DTop	DBot
R1[K/W]	2.22e-014	2.22e-014	0.126	0.159	0.02723
R2[K/W]	0.1142	0.08166	0.07262	0.06656	2.22e-014
R3[K/W]	0.04106	0.02991	0.03267	0.02875	2.22e-014
C1[Wsec/K]	0.01793	0.1146	6.536	6.817	214
C2[Wsec/K]	28.58	21.93	89.35	118.3	0.05002
C3[Wsec/K]	1646	1823	2888	3571	10.02

The Foster network for the IGBT module is as shown in Figure 25.

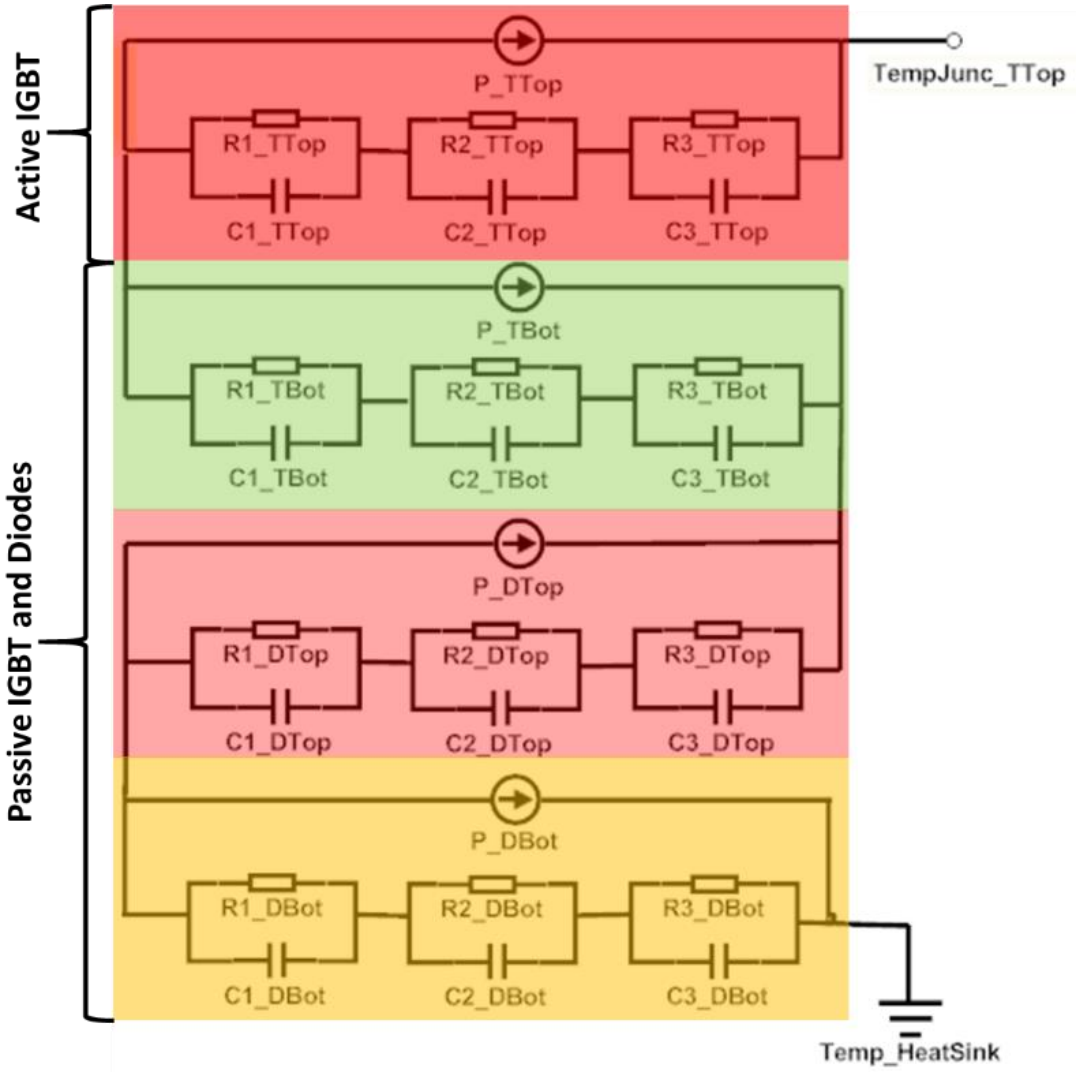

Figure 25: Foster network of active top IGBT

The arrangement of the switching elements in the IGBT module is as follows **TTop, DTop, DBot, TBot**, which means that the top diode is closer to the top IGBT than the bottom diode and IGBT. This explains why the measured temperature and hence thermal impedance in the passive bottom diode for an active top IGBT is higher than those of the passive bottom diode and IGBT.

3.5. Junction Temperature Measurement Using Infrared Camera

The infrared camera of Figure 10 is used in measuring the steady-state junction temperature of the active IGBT or diode. Infrared image for the active top IGBT and active top diode at 5m/s air flowrate are shown in Figure 26 and Figure 27.

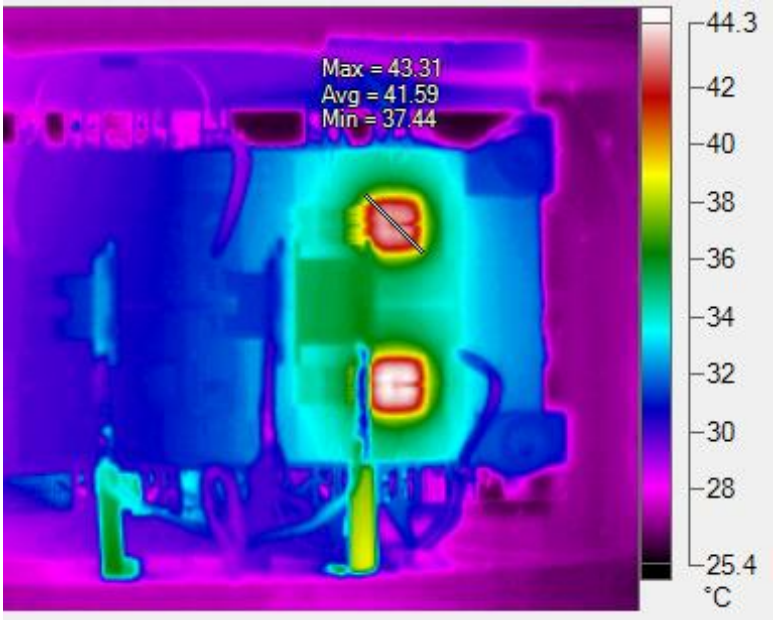

Figure 26: Infrared image of active top IGBT at 5m/s air flowrate

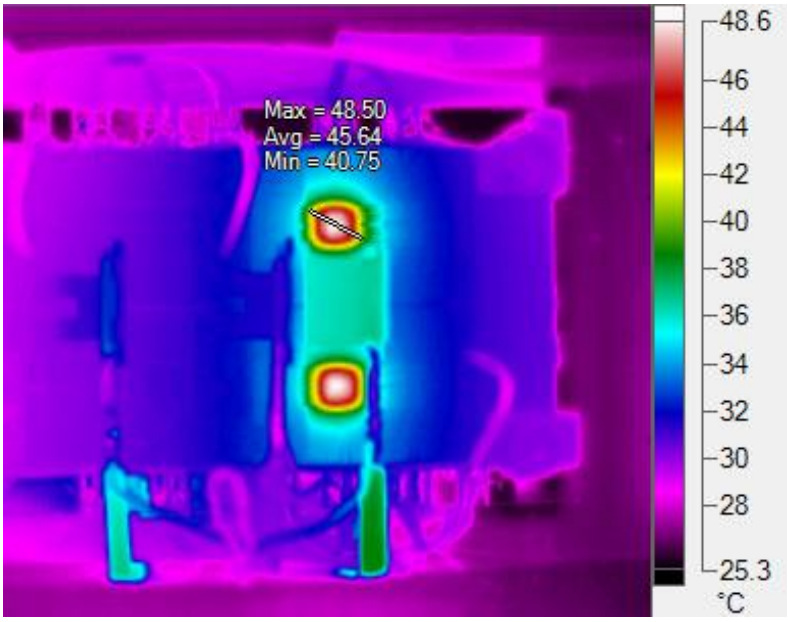

Figure 27: Infrared image of active top diode at 5m/s air flowrate

The active switches have the highest temperatures as expected. The measured temperature profile of both top parallel switches are identical. In order to do derive the virtual junction temperature of the active switching element from the infrared image, the temperature profile of a diagonal line drawn from the edge of the square or rectangular active IGBT or diode through the centre of the switching element is analysed [71]. Temperature profile along the diagonal line in the infrared image in Figure 26 and Figure 27 used in the evaluation of junction temperature are shown in Figure 28 and Figure 29.

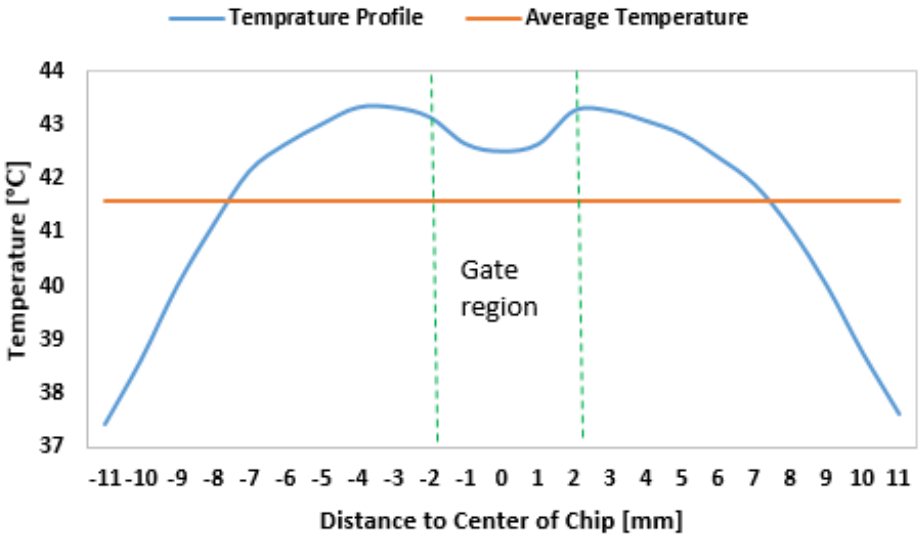

Figure 28: Temperature distribution along diagonal line for active top IGBT at 5m/s air flowrate

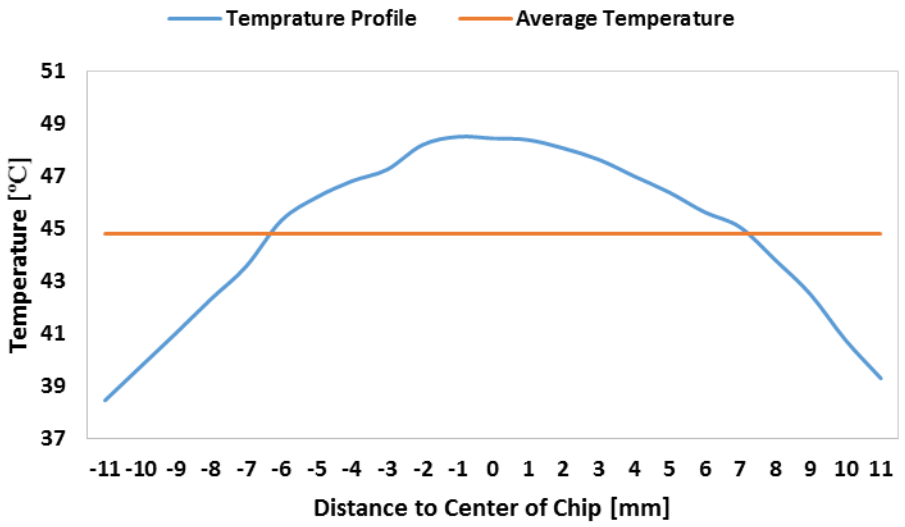

Figure 29: Temperature distribution along diagonal line for active top diode at 5m/s air flowrate

It can be seen from Figure 28 that measured temperature decreases with increase in distance from the centre of the chip (towards -11 or 11mm). Towards the centre of the IGBT as shown in Figure 28 a temperature dip is observed in the gate region also reported in [71] [72].

Maximum, minimum and average temperatures of the active top IGBT at 5m/s and 14m/s air flowrate obtained from the infrared image are compared with direct and voltage-based temperatures as shown in

Table **4**.

Table 4: Comparison of infrared, voltage-based and direct measured temperatures

Flowrate [m/sec]	Temperature[°C]				
	TMax_IR	TMin_IR	TAvg_IR	TTop	TTop_VCE
5	43.31	37.44	41.59	36.35	35.97
14	42.13	37.06	40.81	35.12	34.24
	DMax_IR	DMin_IR	DAvg_IR	DTop	DTop_VF
5	48.44	39.81	45.45	36.57	36.22
14	47.5	40.06	44.93	35.43	34.76

TMax_IR, TMin_IR, TAvg, DMax_IR, DMin_IR, DAvg_IR are steady state maximum, minimum and average temperatures of active top IGBT(T) and top diode(D) measured by the infrared camera. TTop, TTop_VCE, DTop, DTop_VF are direct measure and voltage-based measured temperatures of active top IGBT and diode. As reported in [36], IGBT or diode temperatures measured using the voltage-based temperature method is a representation of the average IGBT or diode junction temperature.

Table **4** represents a validation of the voltage-based and direct temperature measurement methods as it is observed that the difference between the average temperatures measured by the infrared camera and the voltage-based and direct temperature measurement methods is approximately 6°C for the IGBT and 9°C for the diode. These differences are well within an acceptable margin as higher temperature differences between VCE based measurements and infrared measurements under the same operating conditions have been reported in [72].

Table 4 also shows that the maximum IR temperatures for IGBT are in the range of 2 – 3°C higher than the average measured IR temperatures. Under the same operating condition, the diode temperatures are higher than those of the IGBTs which results in higher diode Zth values. The corresponding Zth values based on maximum and average temperature values in

Table 4 values are given in Table 5.

Table 5: Comparison of Zth values from maximum measured infrared temperature, voltage-based and direct measured temperatures

Flowrate [m/sec]	**Zth[K/W]**			
	Zth_TTop	**Zth_TTop_VCE**	**Zth_TAvg_IR**	**Zth_TMax_IR**
5	0.2305	0.2194	0.385231947	0.436019118
14	0.2261	0.2003	0.373395362	0.411871699
	Zth_DTop	**Zth_DTop_VF**	**Zth_DAvg_IR**	**Zth_DMax_IR**
5	0.2634	0.252	0.554759449	0.652865201
14	0.2553	0.2339	0.54776623	0.645995308

The Zth values of IGBT and diodes calculated using the maximum temperatures measured by the infrared camera are higher than their corresponding values calculated from the voltage-based and direct measured temperatures as seen in Table 5 because of the difference in maximum and average measured temperatures reported in

Table 4. The Zth values in Table 5 present very interesting scenarios in the thermal modelling and junction temperature estimation. Thermal models implemented using Zth values calculated from maximum temperatures will be very conservative as the maximum junction temperature for the given operating condition is calculated. Such thermal models are much more suitable in applications where the inverter is operated frequently in near maximum operating junction temperature limits. Better thermal protection and longer lifetime of the IGBT modules are obtained if the thermal management strategy is based on the thermal models using Zth values based on maximum measured temperatures. On the other hand, thermal performance could be greatly limited using Zth values based on maximum temperatures especially in applications where the inverter is not operated frequently in high temperature regions. In this case, the less conservative thermal models using average measured temperatures are much more suitable.

4. Identification of thermal networks using least squares

4.1. Linear transfer function

As an alternative to the conventional method, we study a linear multi-input single-output representation of transfer function between the source of heat and the monitored temperature. For simplicity of notation, we present the model for a single element with temperature T, but it will be later used to model all elements. In discrete time, the temperature T of the mth element evolves as

$$\boldsymbol{T_{m,k}} \;=\; \sum_{i=1}^{\bar{i}} \left(\sum_{l=1}^{\bar{l}} \left(\boldsymbol{a_{m,l,i} T_{l,k-i}} + \boldsymbol{z_{m,l,i} P_{l,k-i}} \right) + \boldsymbol{c_{m,i} T_{\mathrm{bp},k-i}} \right), \qquad 4.1$$

where $\boldsymbol{k = 1 \ldots \bar{k}}$ is the index of the discrete time sample, $\boldsymbol{l = 1 \ldots \bar{l}}$ is the index of active element, the $\boldsymbol{P_l}$ is the instantaneous power input of the $\boldsymbol{l}$th source, $\boldsymbol{l = 1 \ldots, \bar{l}}$. Index $\boldsymbol{i = 1 \ldots \bar{i}}$, denote delays in the temperatures and power inputs. The maximum delay of the data is $\boldsymbol{\bar{i}}$ and the first measurement of the $\boldsymbol{l}$th temperature that can be predicted by model (4.1) is $\boldsymbol{T_{l,\bar{i}+1}}$. Aggregating measurements in the full time series into vectors:

$$\begin{aligned}
\mathbf{T}_{\boldsymbol{l,0}} &= [\boldsymbol{T_{l,\bar{i}+1}}, \ldots, \boldsymbol{T_{\bar{k}}}]^{\top}, \\
\mathbf{P}_{\boldsymbol{l,0}} &= [\boldsymbol{P_{l,\bar{i}}}, \ldots, \boldsymbol{P_{l,\bar{k}-1}}]^{\top}, \\
\mathbf{T}_{\boldsymbol{l,-i}} &= [\boldsymbol{T_{\bar{i}+1-i}}, \ldots, \boldsymbol{T_{\bar{k}-i}}]^{\top}, \\
\mathbf{P}_{\boldsymbol{l,-1}} &= [\boldsymbol{P_{l,\bar{i}+1-i}}, \ldots, \boldsymbol{P_{l,\bar{k}-1-i}}]^{\top},
\end{aligned} \qquad 4.2$$

and contributions from each element into matrices

$$\begin{aligned}
\mathbb{T}_{\boldsymbol{l}} &= [\mathbf{T}_{\boldsymbol{l,-1}}, \mathbf{T}_{\boldsymbol{l,-2}}, \ldots \mathbf{T}_{\boldsymbol{l,-\bar{i}}}], \\
\mathbb{T}_{\mathbf{bp}} &= [\mathbf{T}_{\mathbf{bp,-1}}, \mathbf{T}_{\mathbf{bp,-2}}, \ldots \mathbf{T}_{\mathbf{bp,-\bar{i}}}], \\
\mathbb{P}_{\boldsymbol{l}} &= [\mathbf{P}_{\boldsymbol{l,-1}}, \mathbf{P}_{\boldsymbol{l,-2}}, \ldots \mathbf{P}_{\boldsymbol{l,-\bar{i}}}],
\end{aligned} \qquad 4.3$$

we can rewrite model (3.1) as

$$\mathbf{T}_{\boldsymbol{m,0}} = \sum_{\boldsymbol{l=1}}^{\bar{\boldsymbol{l}}} \left(\mathbb{T}_{\boldsymbol{l}} \mathbf{a}_{\boldsymbol{m,l}} + \mathbb{P}_{\boldsymbol{l}} \mathbf{z}_{\boldsymbol{m,\bar{l}}} \right) + \mathbb{T}_{\mathbf{bp}} \mathbf{c}_{\boldsymbol{m}} \qquad 4.4$$

where vector $\mathbf{a}_{m,l} = [a_{m,l,1}, \ldots a_{m,l,\bar{i}}]^{\top}$, $\mathbf{z}_{m,l} = [z_{m,l,1}, \ldots z_{m,l,\bar{i}}]^{\top}$, and $\mathbf{c}_m = [c_{m,1} \ldots c_{m,\bar{i}}]^{\top}$.

Model (4.4) represent for each element a set of linear equations

$$\mathbf{y}_m = \mathbb{A}\mathbf{x}_m, \tag{4.5}$$

where $\mathbf{y}_m = \mathbf{T}_{m,0}$,

$$\begin{aligned} \mathbb{A} &= [\mathbb{T}_{\mathbf{1}}, \dots \mathbb{T}_{\bar{\boldsymbol{l}}}, \mathbb{P}_{\mathbf{1}}, \dots \mathbb{P}_{\bar{\boldsymbol{l}}}, \mathbb{T}_{\mathbf{bp}}], \\ \mathbf{x}_{\boldsymbol{m}} &= [\mathbf{a}_{\boldsymbol{m},\mathbf{1}}{}^{\top} \dots \mathbf{a}_{\boldsymbol{m},\bar{\boldsymbol{i}}}{}^{\top}, \mathbf{z}_{\boldsymbol{m},\mathbf{1}}{}^{\top} \dots \mathbf{z}_{\boldsymbol{m},\bar{\boldsymbol{i}}}{}^{\top}, \mathbf{c}_{\boldsymbol{m}}^{\top}]^{\top}. \end{aligned} \tag{4.6}$$

Estimation of vector of unknown parameters $\mathbf{x}$ is obtained by minimization of the square error, typically written in the form of L2 norm $||\mathbf{y}_m - \mathbb{A}\mathbf{x}_m||_2^2$. The solution to this problem is the well known least squares

$$\mathbf{x}_{\boldsymbol{m}} = (\mathbb{A}^{\top}\mathbb{A})^{-\mathbf{1}}\mathbb{A}^{\top}\mathbf{y}_{\boldsymbol{m}}, \tag{4.7}$$

where $^{\top}$ denotes transposition of a matrix.

While we assume that the temperature is measured, the measurement of the power input is less clear. If voltage drop on an element is measured, we can obtain good estimate

$$\boldsymbol{P}_{\boldsymbol{l},\boldsymbol{k}} = \boldsymbol{V}_{\boldsymbol{CE},\boldsymbol{l},\boldsymbol{k}}\boldsymbol{I}_{\boldsymbol{l},\boldsymbol{k}}, \tag{4.8}$$

where V_{CE} is a voltage drop, and I_k is the current passing through the lth element. Due to complicated measurement of the voltage drop, only the current is measured and the power is then typically approximated by a second order polynomial

$$\boldsymbol{P}_{\boldsymbol{l},\boldsymbol{k}} = \boldsymbol{\alpha}\boldsymbol{I}_{\boldsymbol{l},\boldsymbol{k}} + \boldsymbol{\beta}\boldsymbol{I}_{\boldsymbol{l},\boldsymbol{k}}^{\mathbf{2}}, \tag{4.9}$$

with coefficients α and β obtained e.g. from data sheet of the module. Note however that after substitution of (4.9) into (4.1) the unknown coefficient z is multiplied by α or β. Thus, we can directly estimate $z_{\alpha,m,l,i} = z_{m,l,i}\alpha$ and $z_{\beta,m,l,i} = z_{m,l,i}\beta$ using the least squares procedure. In that case, the matrix $\mathbb{A}$ is composed of vectors $\mathbb{T}_l$ and $\mathbb{I}_l = [\mathbf{I}_{l,-1}, \dots, \mathbf{I}_{l,-\bar{i}}]$ and $\mathbb{I}_l^2 = [\mathbf{I}_{l,-1}^2, \dots, \mathbf{I}_{l,-\bar{i}}^2]$ where $\mathbf{I}_{l,-i} = [I_{l,\bar{i}+1-i}, \dots, I_{l,\overline{k}-i}]$.

4.2. Computational issues

Note that due to large number of parameters, computation of matrix $(\mathbb{A}^{\top}\mathbb{A})^{-1}$ in (4.7) may become problematic since its smallest eigenvalues typically approach zero. Then, the inverse operation may not be defined. Even if it is defined, the eigenvectors associated with small eigenvalues are typically affected by noise and they are magnified by the inverse operation. Such a situation is a symptom of overfitting, i.e.

fitting a complex model to insufficient number of data. It can be improved by adding more relevant data to the regression. An alternative is to add regularization terms to the optimization.

4.3. Regularizations methods

The most common regularization is known as the ridge regression [73] in which the least squares is complemented by addition of L2 penalization:

$$\hat{\mathbf{x}}_m = \underset{\mathbf{x}_m}{\operatorname{argmin}} ||\mathbf{y}_m - \mathbb{A}\mathbf{x}_m||_2^2 + \alpha||\mathbf{x}_m||_2^2, \qquad 4.10$$

where $\alpha > 0$ is a chosen regularization coefficient, $||\cdot||_2$ denotes $L2$ norm of vector argument, i.e. square root of sum of squares of its elements. The motivation behind this choice is to penalize parameters that are too large (which happens when the data are not informative) [74]. Key advantage of this approach is that it allows for analytical solution, very similar to the original least squares (4.7)

$$\hat{\mathbf{x}}_m = (\mathbb{A}^\top \mathbb{A} + \alpha I)^{-1}\mathbb{A}^\top \mathbf{y}_m. \qquad 4.11$$

However, it remains to choose the tuning coefficient α, which is often done by the cross-validation method.

An alternative to ridge regression is the Least Absolute Shrinkage and Selection Operator (LASSO) introduced in [75]. It is very similar to the ridge regression but optimizing L1 penalization instead of L2:

$$\hat{\mathbf{x}}_m = \underset{\mathbf{x}_m}{\operatorname{argmin}} ||\mathbf{y}_m - \mathbb{A}\mathbf{x}_m||_2^2 + \alpha||\mathbf{x}_m||_1, \qquad 4.12$$

where $||\cdot||_2$ denotes $L1$ norm of vector argument, i.sum of absolute values of its elements. The penalization coefficient α has the same role as for the ridge regression. The disadvantage of this method is that it doe not have an analytical solution but has to be optimized numerically. Key advantage is that the solutions obtained by this method are sparse, i.e. the redundant parameters are estimated to be zeros. Thus even a higher order model can have few parameters which is advantageous for real-time implementation. The problem of selection of the tuning coefficient is identical to that of the ridge regression.

An alternative method that does not require tuning is the Relevance Vector Machine [76]. It is based on iterative evaluation of (4.11) which is thus more computationally demanding. However, it prefers sparse solutions (i.e. zero coefficient of model (4.1) which may be interesting property for real time implementation. Moreover, it does not suffer from large biases as the LASSO method.

4.4. Tuning of penalizations

While many methods for selection of the tuning coefficients are available, e.g. the L-curve method, we will use properties of our problem for its selection. Specifically, we aim to predict the temperatures T in the regressor of model (4.1) using only predictions of previous values,

$$\widehat{\boldsymbol{T}}_{\boldsymbol{m,k}} = \sum_{\boldsymbol{i=1}}^{\bar{\boldsymbol{i}}} \left(\sum_{\boldsymbol{l=1}}^{\bar{\boldsymbol{l}}} \left(\boldsymbol{a}_{\boldsymbol{m,l,i}} \widehat{\boldsymbol{T}}_{\boldsymbol{l,k-i}} + \boldsymbol{z}_{\boldsymbol{m,l,i}} \boldsymbol{P}_{\boldsymbol{l,k-i}} \right) + \boldsymbol{c}_{\boldsymbol{m,i}} \boldsymbol{T}_{\mathbf{bp},\boldsymbol{k-i}} \right), \tag{4.13}$$

where the key change from (4.1) is replacement of the delayed measurements $T_{l,k-i}$ by delayed predictions $\hat{T}_{l,k-i}$. The error of prediction is thus accumulating and incorrect parameters yields large prediction error, $e_{m,k} = \hat{T}_{m,k} - T_{m,k}$. Therefore, we can consider this error as a cross validation metric. Specifically, we will consider two evaluation metrics on $e_{m,k}$: the mean square error and maximum error

$$\begin{aligned} \mathrm{mse}(e_m) &= \frac{1}{M} \sum_{m=1}^{M} \frac{1}{K} \sum_{k=1}^{K} e_{m,k}^2 , \\ \max(e_m) &= \max_{k=1..K, m=1..M} e_{m,k}. \end{aligned} \tag{4.14}$$

The former is used due to its relation to the training error, the latter is used due to application interest. In many application, the temperature is checked not to reach its maximum value. Hence, it is important to be safe and keep the safety margin related to the maximum of the estimation error. For consistency of the metrics, we also average over all power element (index m) in the former, and find maximum over all power elements in the latter.

Note that we have measurements under several experimental conditions differing in cooling speed and active current. We will use different experimental conditions for cross-validation, i.e. we will train the model parameters under one experimental conditions and evaluate its error in all other conditions.

5. Experimental Resultsα

5.1. Experimental Results with Least Squares method

From the set of experiments described in Section 3, we used data recorded at 1m/s flowrate and both steady state currents (25 and 50A) as the training data. The remaining data sets are used for validation of accuracy of the method. We aim to validate accuracy of the method with growing order of the model and sensitivity of the results to the method evaluating the power input. However, as a first step we need to determine the value of the regularization coefficient α.

5.1.1. Penalization Tuning

We have estimated parameters of the tenth-order model on the training data sets (1m/s 25A and 1m/s 50A) and evaluated predictive temperatures (4.13) on all datasets as shown in Figure 30 to Figure 41.

Note that for the tested model, the results are rather insensitive to tuning of $\alpha < 1$ and start deteriorating for higher values. We have tested the RVM method with similar results, see later results. However, the number of coefficients estimated to be zero is less than 10% which is too few for significant computational savings. The prediction errors obtained by the LASSO regularization (both maximum and mean square) as shown in Figure 32 and Figure 33 are slightly higher than those obtained by the ridge regression as shown in Figure 30 and Figure 31. Therefore, we will use the ridge regression with $\alpha = 1$ in the future experiments.

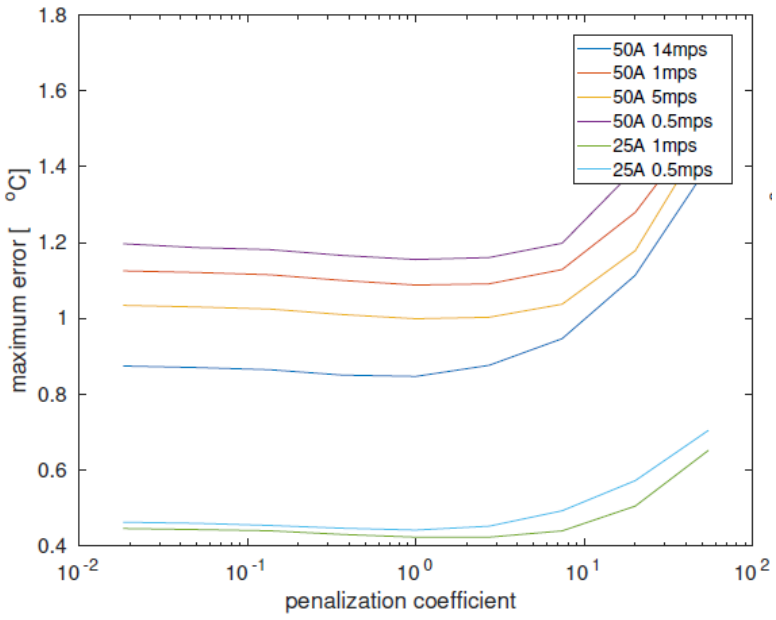

Figure 30: Selection of the regularization coefficient α of the ridge regression using cross-validation for the Foster model of tenth order, maximum error

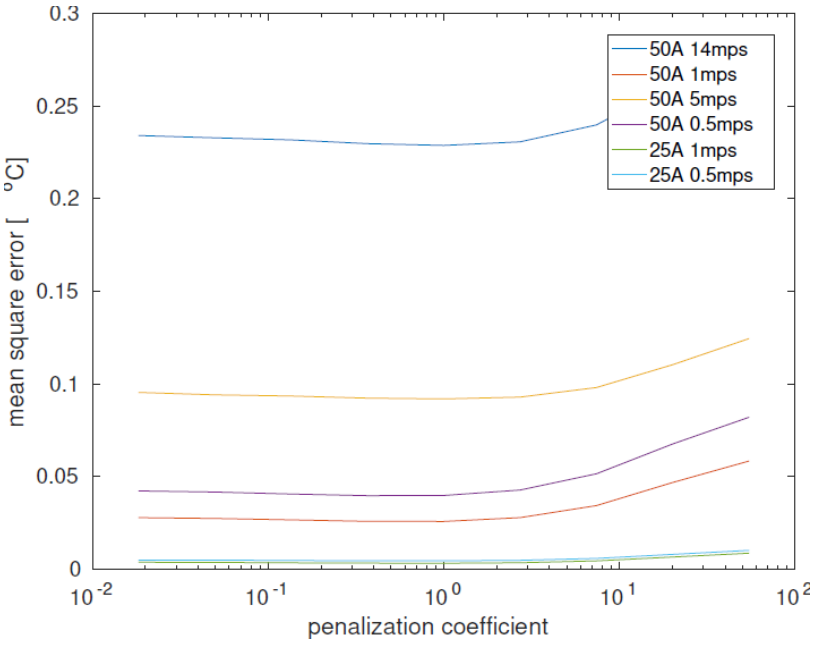

Figure 31: Selection of the regularization coefficient α of the ridge regression using cross-validation for the Foster model of tenth order, mean square error

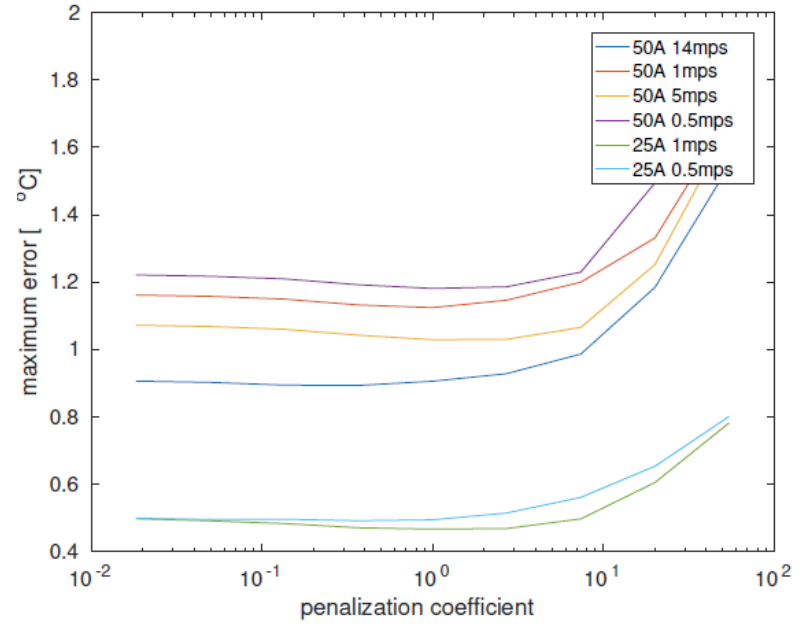

Figure 32: Selection of the regularization coefficient α of LASSO using cross-validation for the Foster model of tenth order, maximum error

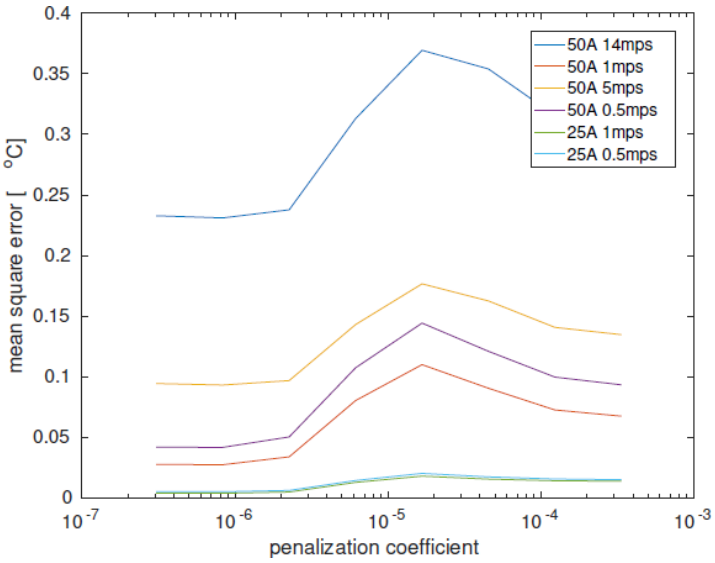

Figure 33: Selection of the regularization coefficient α of LASSO using cross-validation for the Foster model of tenth order, mean square error

The maximum error of prediction (maximum over time as well as all elements in the module) is displayed in Figure 34 for I^2 power model and Figure 35 for IU power model. In both cases $\alpha = 1$ seems to be a good choice

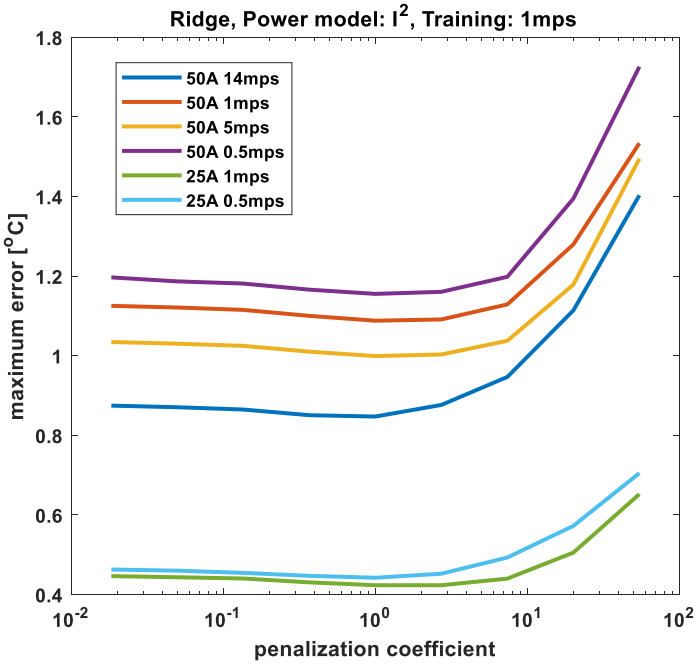

Figure 34: Maximum error vs penalization coefficient ridge regression for I^2 power model

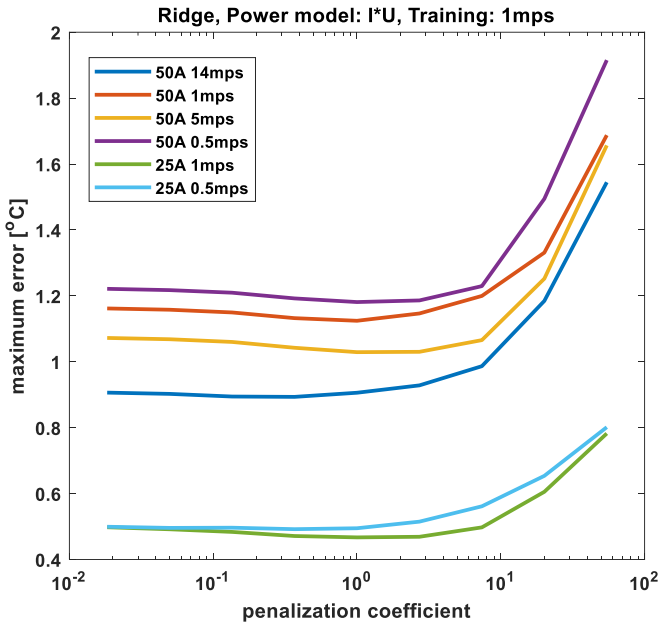

Figure 35: Maximum error vs penalization coefficient ridge regression for UI power model

5.1.2. Model Order

With selected penalization of the regularization, we have tested sensitivity of the maximum prediction error to the order of the linear model (3.1). A comparison of the variation of maximum error with model order for the ridge and RVM models are shown in Figure 36 and Figure 37. It can be observed from both figures that the ridge regression yield slightly better results than the RVM for the same training data set

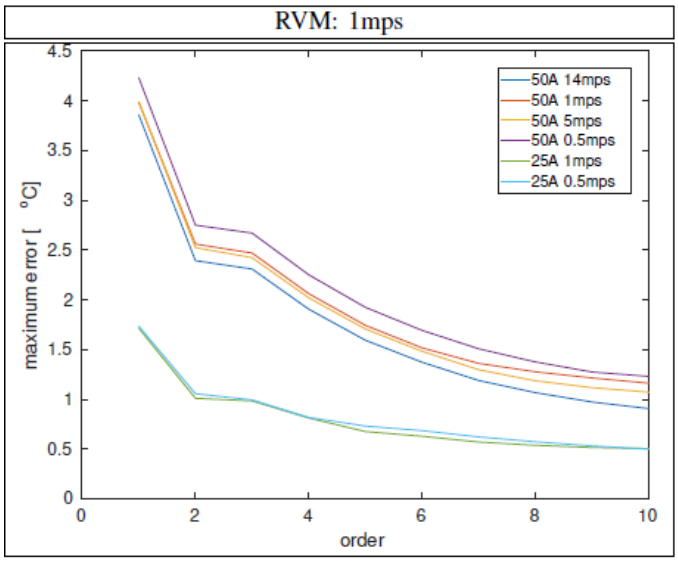

Figure 36: Maximum error vs model for I^2 power model RVM training at 1mps

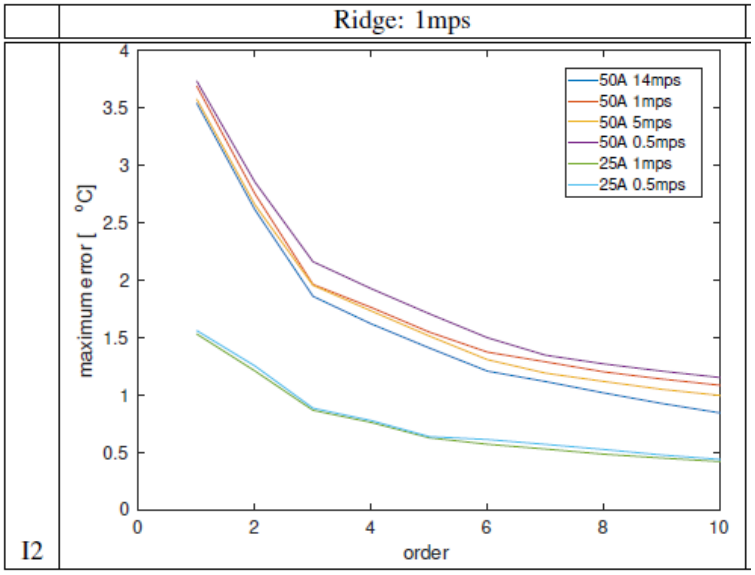

Figure 37: Maximum error vs model for I^2 power model ridge regression training at 1mps

The results for the I^2 power model of ridge regression are displayed in Figure 38 and for the IU power model in Figure 40. Note that the profile is almost the same for both power models. The prediction error is monotonically decreasing with the model order, reaching a plateau for orders higher than 5. This result is due to good selection of the regularization coefficient α.

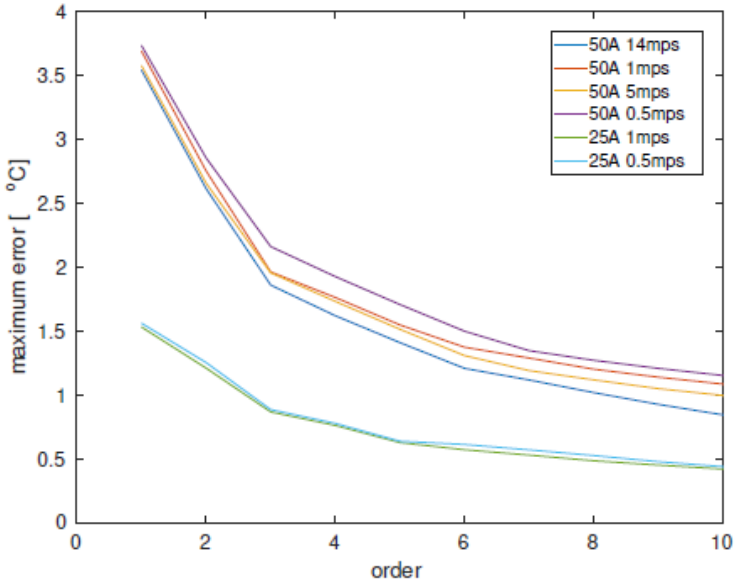

Figure 38: Maximum error vs model order least squares for I^2 power model at 1mps training

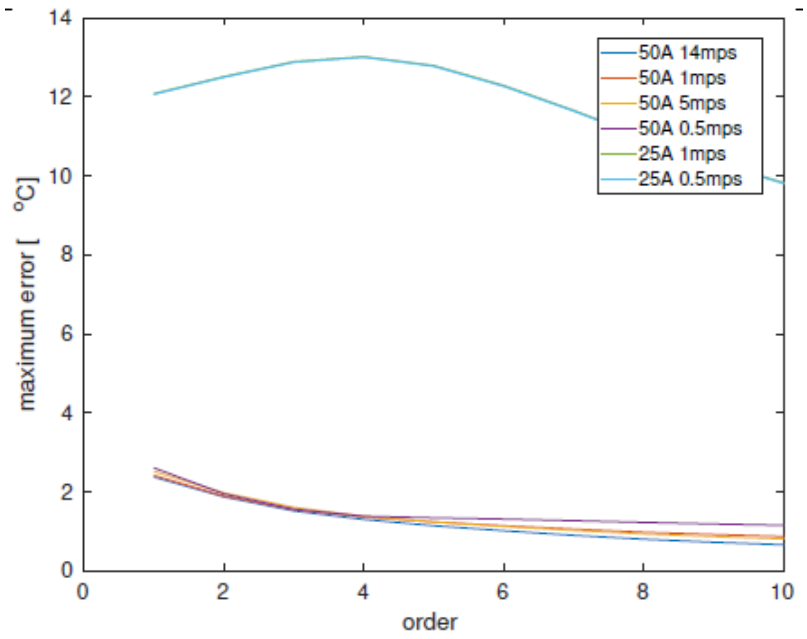

Figure 39: Maximum error vs model order least squares for I^2 power model at 5mps training

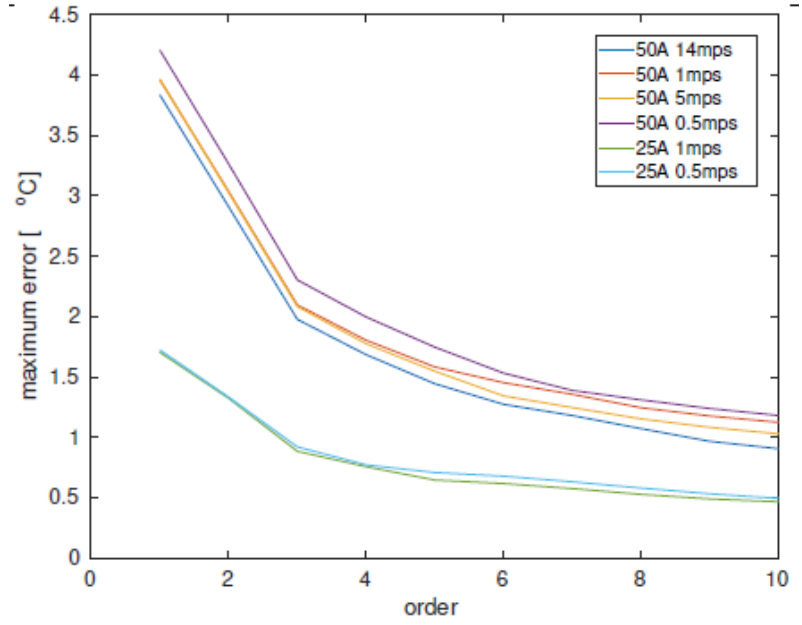

Figure 40: Maximum error vs model order least squares for UI power model at 1mps training

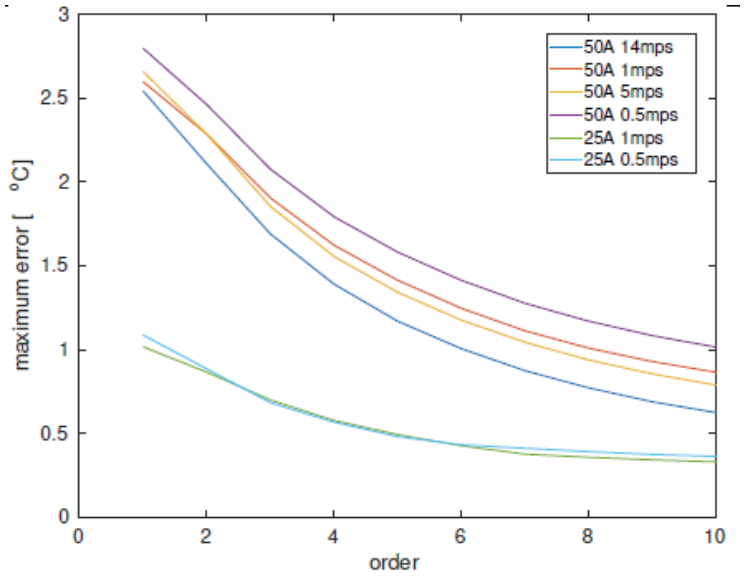

Figure 41: Maximum error vs model order least squares for UI power model at 5mps training

As can be seen from Figure 38 to Figure 41 the best results for both the I^2 and UI methods are obtained with training data at 1mps. It is therefore imperative to select a suitable training data for the model.

The 3rd order modelled top transistor temperature (model equation (4.12)) and measured top transistor temperatures with $\alpha = 1$ is shown in Figure 42.

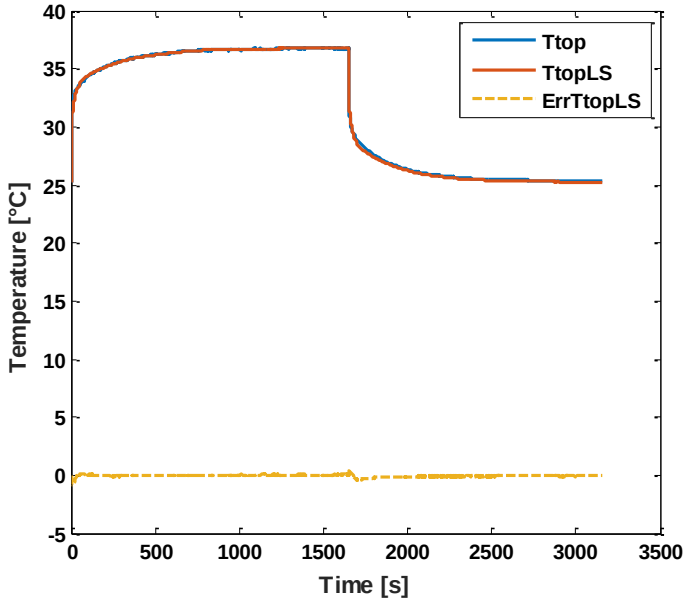

Figure 42: Measured vs least-squares model temperature 3rd order top transistor active 50A 5m/s air flowrate

5.2. Experimental Results with TSEP method

Though the temperature distribution is assumed to be homogenous in the cool down phase, a discrepancy was observed in the temperatures measured from the heat sink sensor as well as those from the 8 sensors placed closed to the transistors and diodes as shown in Figure 43. Since the sensors were all of type Pt100, it is important to consider this discrepancy in the determination of the calibration curve. Hence two calibration curves to establish the linear relationship between voltage and temperature are determined; one based on the maximum of the measured temperatures and the other based on the average values of the measured temperatures in the cool down phase as shown in Figure 44.

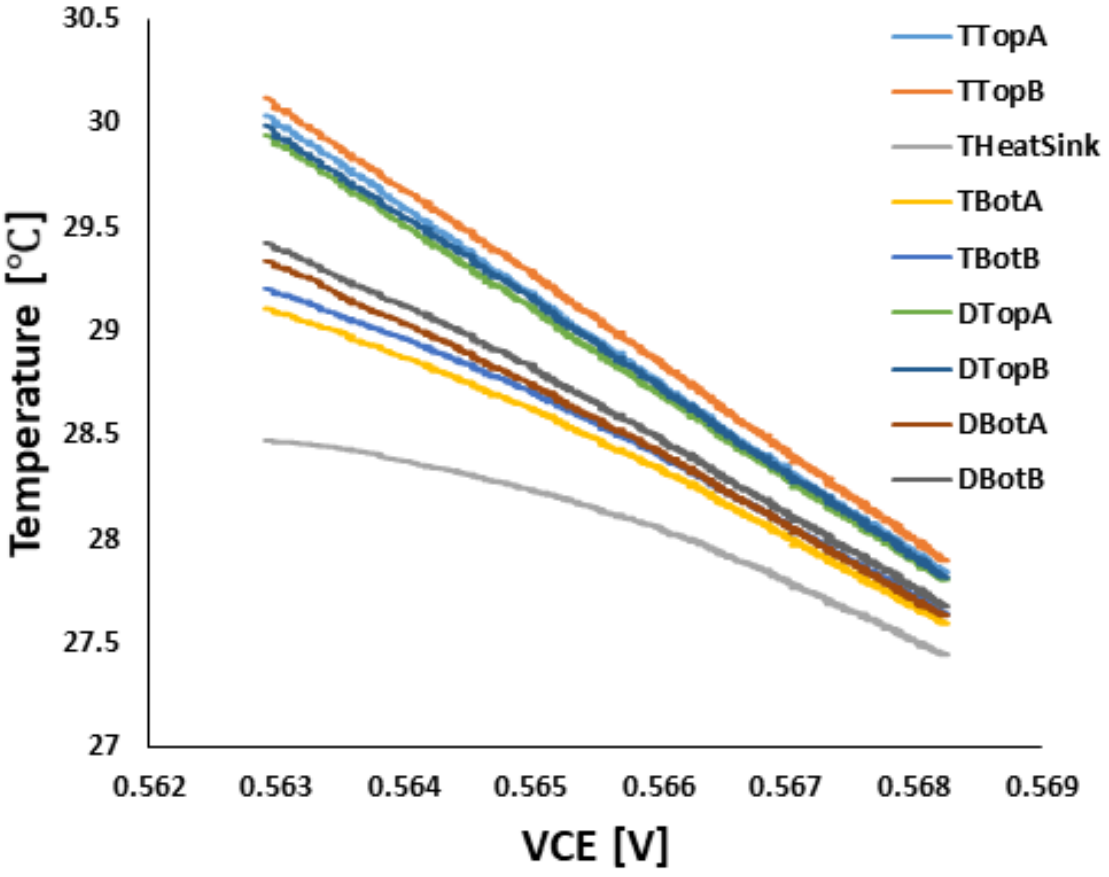

Figure 43: Measured temperatures in cool-down phase

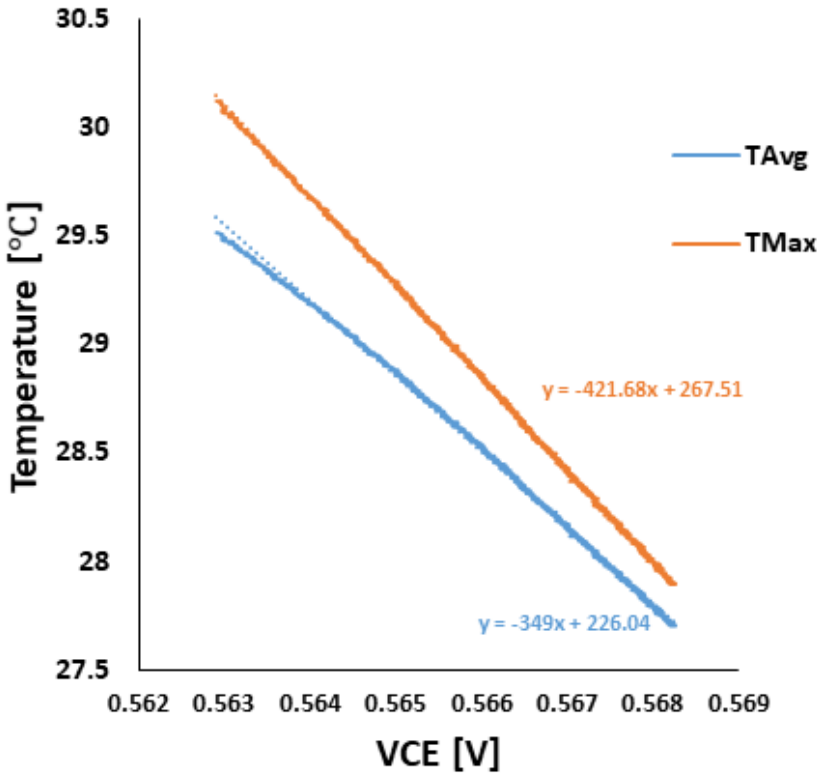

Figure 44: Calibration curves determined from maximum and average temperatures

The thermal impedance network obtained using the maximum and average values of temperature yield slightly different results.

Calibration curves for maximum and average measured temperatures are used in recomposing the junction temperatures for the transistors and diodes. As described in [49], the thermal impedances and capacitances are extracted by curve fitting methods from equation (2.10). By placing the temperatures sensor closed to the transistors and diodes in the open IGBT module, the measured temperature is close to the junction temperature as observed by the infrared camera. Hence the measured temperatures are also used in establishing a thermal impedance network from which the junction temperature can be modelled.

Figure 45 shows maximum error against model (2.10) order for different currents and flowrates for which the calibration curve for determining the thermal impedance network is obtained from the average of all measured temperatures in the cool down phase as shown in Figure 44. Figure 46 shows maximum error against model (2.10) order for different currents and flowrates for which the calibration curve for determining the thermal impedance network is obtained from the maximum of all measured temperatures

in the cool down phase as shown in Figure 44. Figure 47 shows maximum error against model (2.10) order for different currents and flowrates for thermal impedance network determined from measured temperatures in the cool down phase as shown in Figure 44.

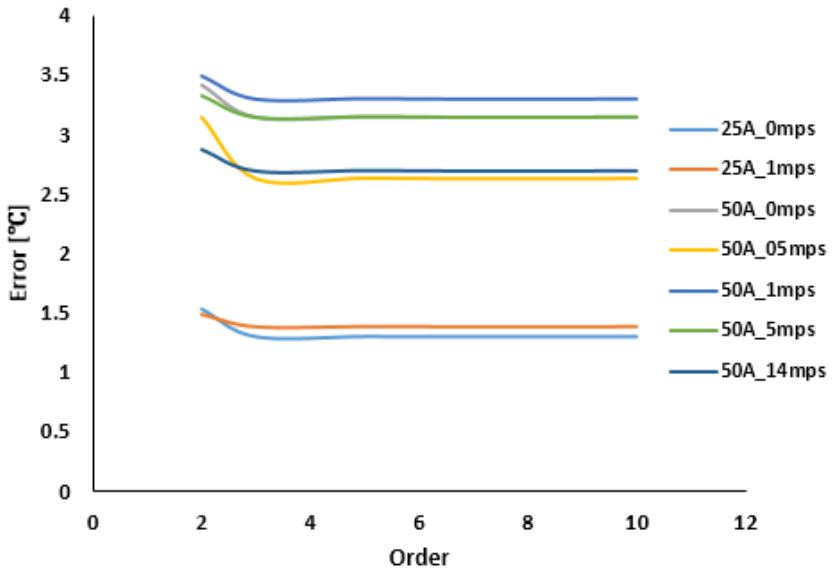

Figure 45: Maximum error vs model order for VCE method with calibration curve from average temperature in cooldown phase

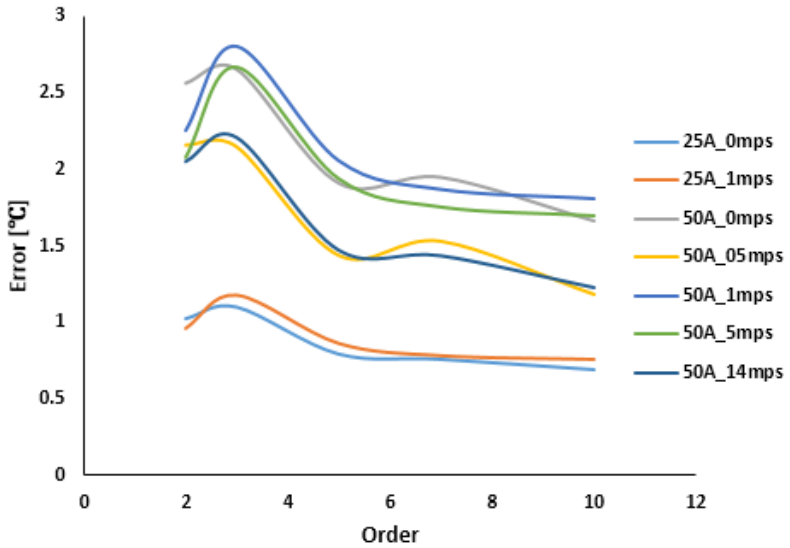

Figure 46: Maximum error vs model order for VCE method with calibration curve from maximum temperature in cooldown phase

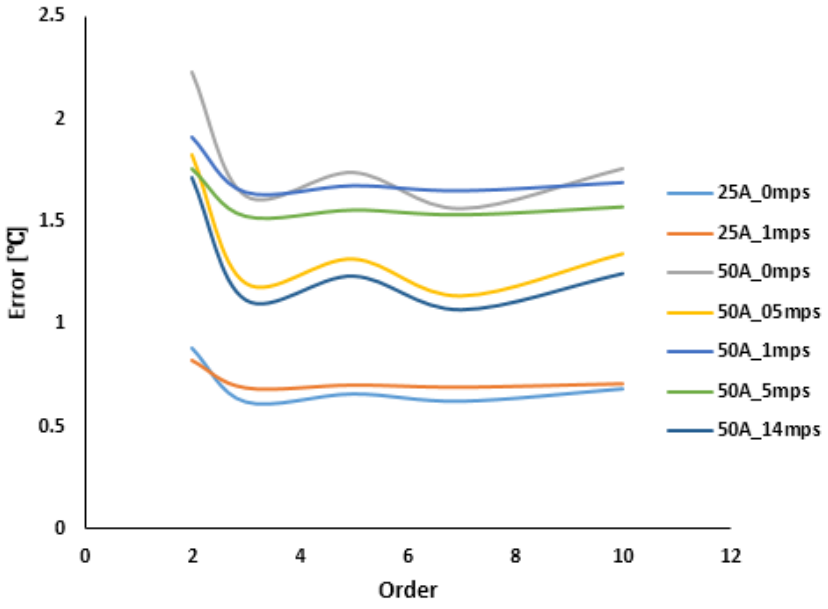

Figure 47: Maximum error vs model order for measured Pt100 temperatures

An important observation from Figure 45, Figure 46 and Figure 47 is that, increasing the model order above 3 does not lead to significant improvements in the maximum and steady state errors. This is important for implementation of a micro controller for real-time calculation of junction temperature where the processor throughput might be an issue.

The results obtained from all three thermal impedance networks (average VCE based, maximum VCE based and measured Pt100 temperature based) for a 3rd order model (2.10) at a flowrate of 5m/s are as shown in Figure 48. TTop is the measured top transistor temperature using the Pt100 sensor. TTopMax is the temperature estimated using the thermal impedance based on the calibration curve using maximum of measured temperatures. TTopAvg is the temperature estimated using the thermal impedance based on the calibration curve using average of measured temperatures. TTopMod is the temperature modelled from the thermal impedance determined from TTop. ErrMod is the difference between TTop and TTopMod, ErrMax is the difference between TTopMax and TTop, ErrAvg is the difference between TTopAvg and TTop.

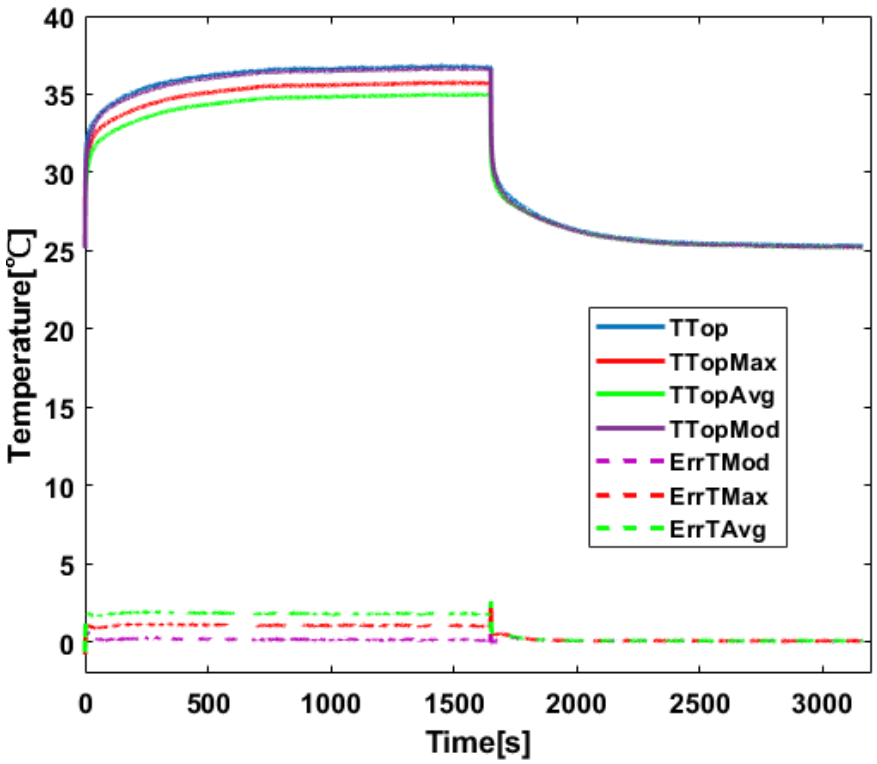

Figure 48: Measured vs model temperatures 3rd order top transistor active 50A 5m/s air flowrate

As shown in Figure 48 the maximum steady state error is observed from the modelled temperature using the average value calibration curve. Maximum error is observed during the transition to the cooldown phase at the point when the transistor or diode is turned off. Steady state errors between measured and model temperatures are within 1℃ which confirms the accuracy of the models. In this paper, we focus not only on the maximum and steady state errors from the modelling, but we also investigate the effect of model complexity (model order) against the maximum error. Since we define the thermal network as a multiple of 1st order systems connected in series the model order in this case is defined as the number of first order systems required by the thermal impedance network to accurately model the required junction temperature.

5.3. TSEP Method vs Novel Least Squares Approach

Validation of modelled junction temperatures with direct measured temperatures with sensors placed close enough to active transistors or diodes is a common industrial practice. Manufacturers usually provide inverters with these capabilities in the product development phase. The proposed least squares based approach provides a better alternative approach to determining the junction temperature from such

inverters. This approach eliminates the sources of error from the TSEP based VCE methods which rely heavily on the accuracy of the measured voltages across the transistors and diodes as well as those measured temperatures in the cooldown phase. Further sources of errors could result from the reconstruction of temperatures from the calibration curve which are later used in the determination of the thermal impedance network.

Under the same operating conditions, the least squares method performs best with maximum temperature error of about 1.2 ℃. On the other hand the TSEP method based on the calibration curve determined from average measured temperatures in the cool down has a maximum temperature error of 2℃ while does of the TSEP method based on calibration curve determined from the maximum measured temperatures in the cool down phase has a maximum temperature error of 3.5℃.

6. Inverter Derating

Derating of electrical drive is essential in safe operation and maximization of the system capabilities [3] [77]. In this thesis, the focus is not limited to maximization and safe operation of the electric drive system. We also get into comfort operation of the electric drive system which is rarely discussed in literature. The derating strategies proposed in the next chapters will address the conventional implementations and also make improvements on the state of the art derating methods with respect to comfort safe operation of the electrical drive system.

6.1. Linear Derating

Instantaneous and adaptive based linear derating discussed in [3] are presented in the next section.

6.1.1. Instantaneous Derating

The instantaneous derating strategy is illustrated in Figure 49.

$T_{Jnc,Lim1}$ is temperature at which linear derating starts (safe operating threshold temperature).

$T_{Jnc,Lim2}$ is the maximum allowed operating junction temperature.

For inverter junction temperature below $T_{Jnc,Lim1}$, operation at maximum current I_{Max} (maximum allowed current limited by system boundary) is allowed. Above $T_{Jnc,Lim1}$, current limit is reduced linearly from I_{Max} to I_{Min} (defined minimum current for continuous operation of the system before safe state activation) for corresponding junction temperature increase from $T_{Jnc,Lim1}$ to $T_{Jnc,Lim2}$ using a fixed gradient defined by

$$\boldsymbol{m = \frac{I_{Max} - I_{Min}}{T_{Jnc,Lim1} - T_{Jnc,Lim2}}} \qquad 6.1$$

If junction temperature continues to increase above $T_{Jnc,Lim2}$ at I_{Min}, the system safe state operation is activated to prevent damage of the inverter. Instantaneous derating works well at high coolant flow rates and high speed operations where a very high currents close to I_{Max} are required to increase the junction temperature above $T_{Jnc,Lim1}$. At low coolant flow rates, very low currents are sufficient to increase the junction temperature above $T_{Jnc,Lim1}$. Instantaneous derating will react too late to the fast temperature rise causing abrupt current reduction which might result to drivetrain oscillations [41] or even safe state activation without derating. Further, if a filter is used to filter the junction or coolant temperature, this will

introduce delays which might result in the inverter being operated above the maximum allowed operating junction temperature using instantaneous derating strategy.

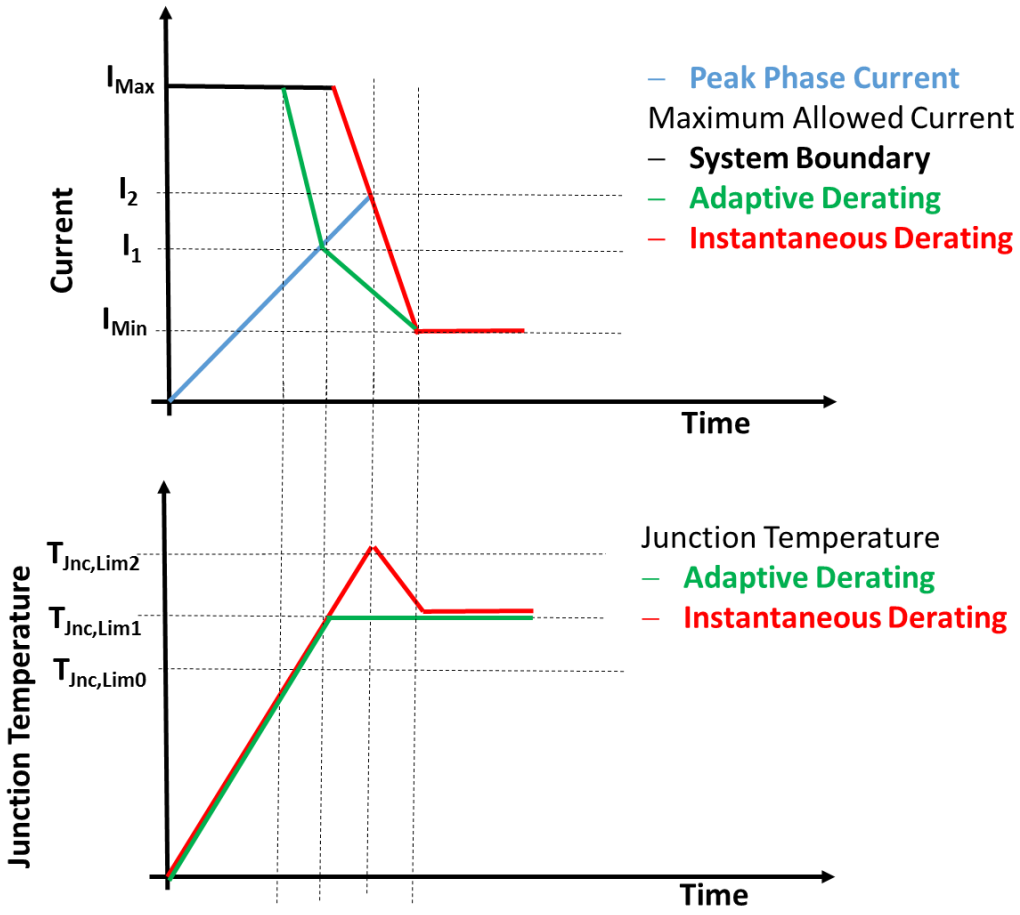

Figure 49: Instantaneous vs adaptive linear derating at low coolant flow rate [3]

6.1.2. Adaptive Derating

6.1.2.1. Peak Phase Current based Adaptive Derating

A simple adaptive derating strategy as shown in Figure 49 is proposed, to resolve the shortcomings of instantaneous derating using the following adaptation rules:

- A temperature limit $T_{Jnc,Lim0}$ is defined below which I_{Max} is allowed.
- Above $T_{Jnc,Lim0}$ the maximum current required to cause the temperature to rise to $T_{Jnc,Lim1}$, is calculated from $T_{Jnc,Inv}$, I_{Max} and the peak phase current (I_{Peak}).

- At temperature limit $T_{Jnc,Lim1}$, the maximum allowed inverter current is I_{Peak}.

The peak phase current $I_{Peak(t)}$ and maximum junction temperature $T_{Jnc,Inv(t)}$ both vary with time.

The maximum allowed current due to adaptive derating $I_{MaxAdap}$ is calculated from $T_{Jnc,Inv}$ as

$$\boldsymbol{I_{MaxAdap(t)} = m(t) * T_{Jnc,Inv(t)} + c(t)} \quad 6.2$$

Constants m and c in the equation for $I_{MaxAdap}$ are calculated from the adaptation rules as follows:

- At $T_{Jnc,Inv} = T_{Jnc,Lim0}$, $I_{MaxAdap} = I_{Max}$
- At $T_{Jnc,Inv} = T_{Jnc,Lim1}$, $I_{MaxAdap} = I_{Peak}$

$$\boldsymbol{m(t) = \frac{I_{Max} - I_{Peak(t)}}{T_{Jnc,Lim0} - T_{Jnc,Lim1}}} \quad 6.3$$

$$\boldsymbol{c(t) = I_{Max} - m(t) * T_{Jnc,Lim0}} \quad 6.4$$

m(t) and *c(t)* are both time varying as there depend on $I_{Peak(t)}$.

The Simulink model of Figure 50 is used to validate the proposed strategy.

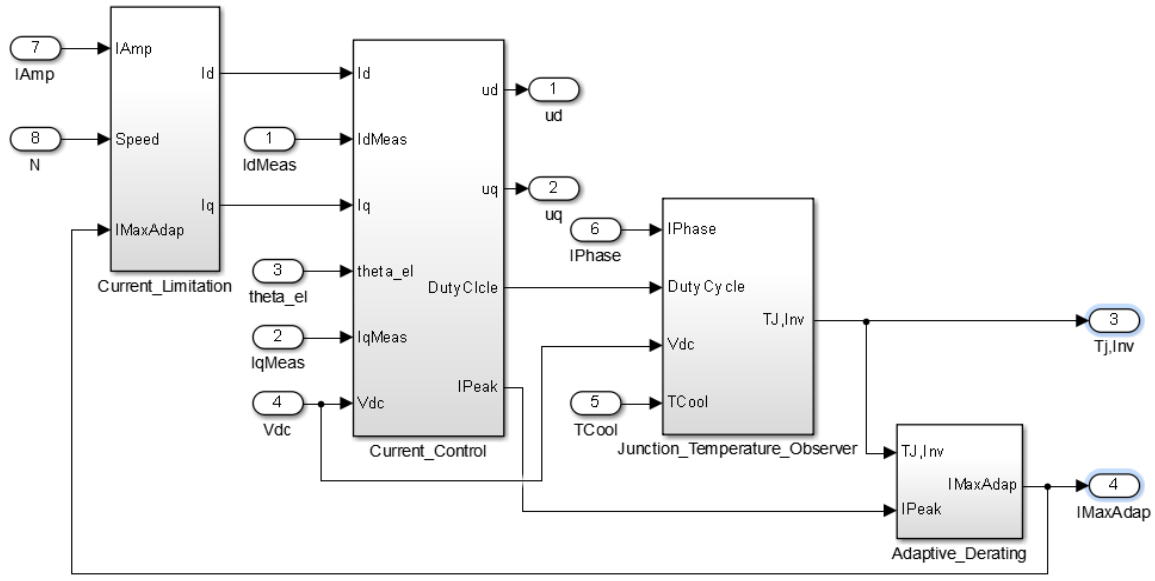

Figure 50: Adaptive derating: Simulink validation

The validation model consists of simple current controller which generates the necessary pwm signals required to control the drive, a junction temperature observer which estimates the junction temperature and a reference current limitation which limits the reference current to the maximum value calculated by the adaptive derating.

$T_{Jnc,Lim0}$ = 120°C because temperatures below 120°C do not pose any thermal stress. $T_{Jnc,Lim1}$ =140°C to allow for a 10°C buffer to the maximum operating junction temperature 150°C. The dc voltage is set at 360V, speed of 2500 rpm (high speed where frequency reduction is deactivated for most applications) and initial coolant temperature of 70°C.

Figure 51 is obtained by plotting maximum values of phase currents required to cause the $T_{Jnc,Inv}$ to increase to $T_{Jnc,Lim1}$ at various coolant flow rates. As expected, the current required to cause $T_{Jnc,Inv}$ to increase to $T_{Jnc,Lim1}$ increases with increase in coolant flow rate. No considerable current improvement is observed for flow rates between 6 and 10L/Min (only about 50A). Hence increasing the coolant flow rate above 6L/Min increases the requirement on the water pump without any meaningful improvement with respect to the maximum possible current. Even at 0L/Min currents below 100A at 2500 rpm are possible without causing $T_{Jnc,Inv}$ to increase above $T_{Jnc,Lim1}$.

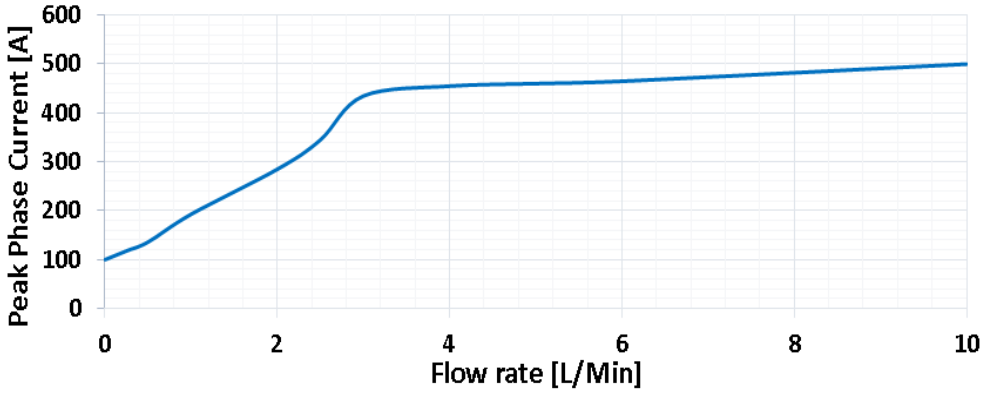

Figure 51: Variation of peak phase current required to cause junction temperature increase to 140°C with flow rate

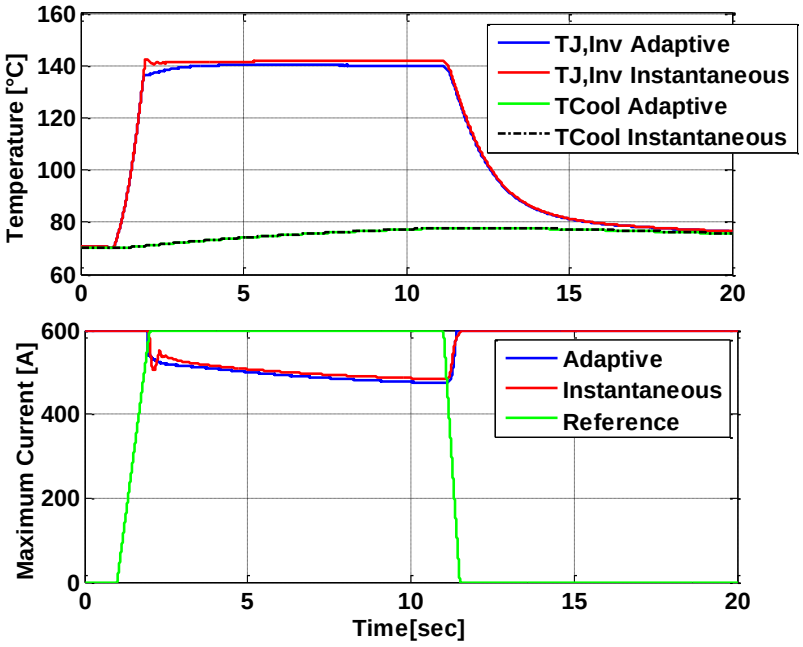

Figure 52: Instantaneous vs adaptive linear derating at 2500 rpm and 6L/Min coolant flow rate

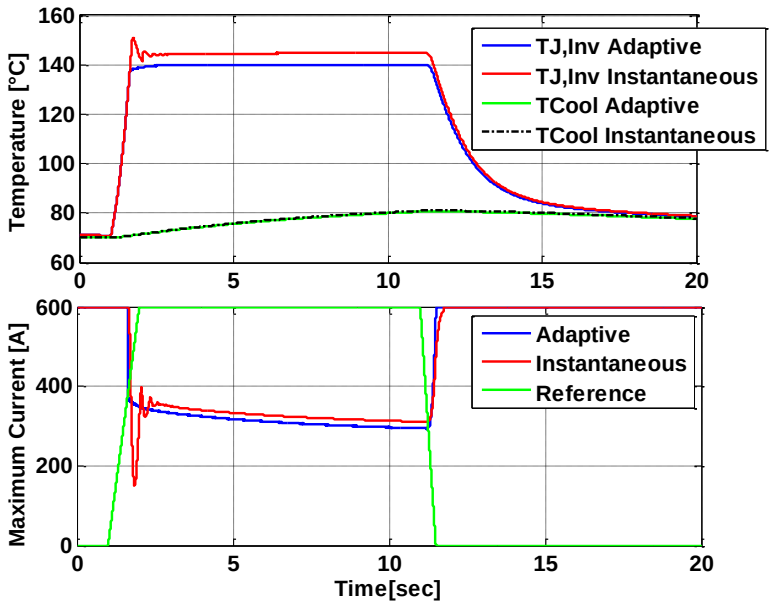

Figure 53: Instantaneous vs adaptive linear derating at 2500 rpm and 2L/Min coolant flow rate

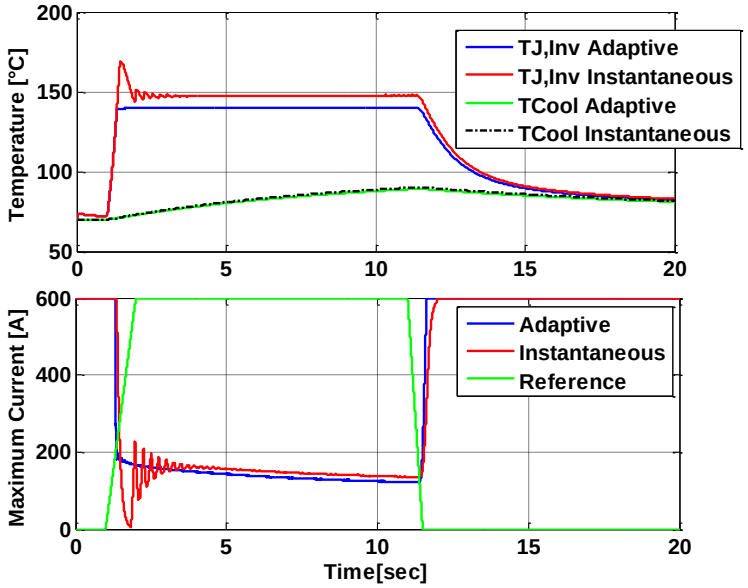

Figure 54: Instantaneous vs adaptive linear derating at 2500 rpm and 0.25L/Min coolant flow rate

There is no noticeable difference between the two derating strategies at high coolant flow rate as seen from Figure 52. Very high currents are required to cause $T_{Jnc,Inv}$ to increase above $T_{Jnc,Lim1}$. This current is close to the maximum current (I_{Max}) which is the reference for instantaneous derating.

The peak phase current required to cause $T_{Jnc,Inv}$ to increase above $T_{Jnc,Lim1}$ is low at low coolant flow rate (Figure 53). Instantaneous derating reacts late to fast temperature increase. $T_{Jnc,Inv}$ increases close to $T_{Jnc,Lim2}$ and the current is reduced rapidly to force the $T_{Jnc,Inv}$ back to $T_{Jnc,Lim1}$, thereby causing oscillations in the derating current. The proposed adaptive derating starts at $T_{Jnc,Lim0}$, react on time to the fast temperature increase. $T_{Jnc,Inv}$ settles at $T_{Jnc,Lim1}$ without any oscillations in current.

Figure 54 depicts system shutdown without derating at near 0L/Min flow rates where instantaneous derating reacts too late and the $T_{Jnc,Inv}$ rises above $T_{Jnc,Lim2}$ before derating starts. Again, the proposed adaptive derating strategy reacts robust to this extreme condition allowing maximum possible current as well as the $T_{Jnc,Inv}$ to settle at $T_{Jnc,Lim1}$.

6.2. I^2t Derating

I^2t derating protects the phase cables from rapid ageing (due to degradation of insulation of the phase cables) [78]. The maximum allowed energy loss resulting from current flow through the cable can be described by

the I^2t limit. Operating the cable out of this limit results in rapid ageing of the cable. Hence I^2t derating ensures that the system is always operated within the I^2t limit.

6.2.1. I^2t Limit Calculation

Every electric drivetrain is characterized by a maximum allowed phase current and a duration for which this maximum current is allowed. Another important system information is the continuous current, which is defined as a current below the allowed maximum current at which the system can be operated continuously without exceeding its I^2t limit. The I^2t limit of the system is calculated from the maximum allowed current I_{Max}, its duration t_{Max} and the continuous current I_{Con} as follows:

$$\boldsymbol{I^2t_{Lim} = \left(I_{Max}^2 - I_{Con}^2\right) * t_{Max}} \qquad 6.5$$

The maximum duration for which peak phase currents I_{Peak} above I_{Con} can be allowed without exceeding the I^2t limit of the system is calculated as follows:

$$\boldsymbol{t_{Lim} = \frac{\left(I_{Max}^2 - I_{Con}^2\right) * t_{Max}}{I_{Peak}^2 - I_{Con}^2}} \qquad 6.6$$

I_{Max} and I_{Con} for the analysis are defined as 600A and 400A (both peak values) respectively. The maximum duration for allowed peak phase currents above the continuous current is as shown in Figure 55 below:

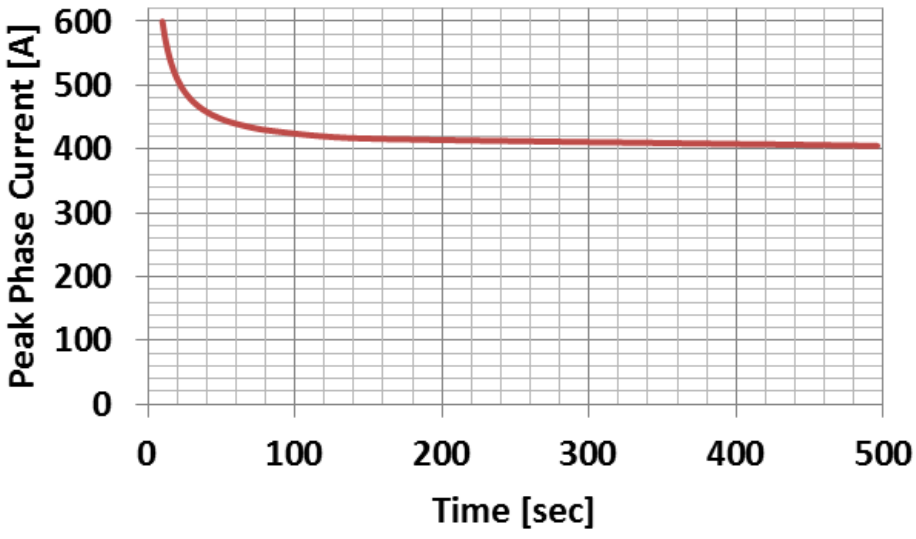

Figure 55: I^2t derating curve

6.2.2. I^2t Counter

I^2t counter is used in calculating the maximum allowed duration for peak phase currents above I_{Con}. Once the I^2t limit is reached, the peak phase current is reduced to the continuous current value according to the I^2t curve shown in Figure 55. If the current demand falls below I_{Con} the maximum allowed current due to I^2t derating is gain reset back to I_{Max} with a rate configured by the I^2t counter. In this paper, the I^2t counter is configured such that the maximum current reset rate depends on the value of current demand below I_{Con}. The maximum current reset duration is at least four times that of the current reduction for the given configuration.

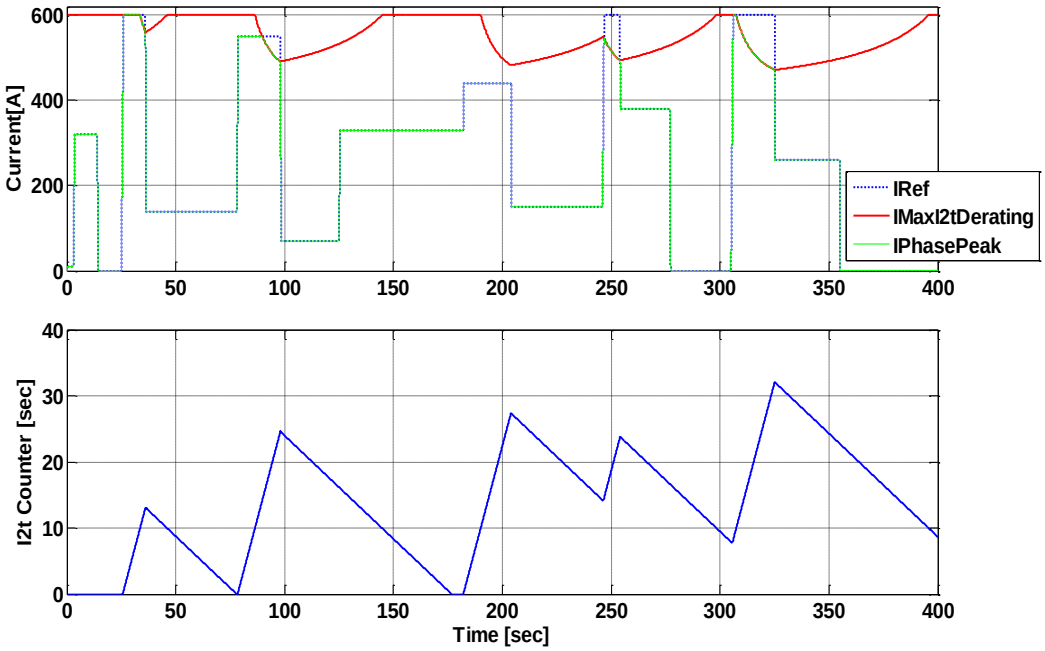

Figure 56: Illustration I2t derating

6.3. Predictive Derating

The actual maximum allowed current considering the states of linear and I^2t derating as well as the maximum allowed current looking 10, 30 and 60 seconds to the future is predicted. The thermal time constants of the Zth network for the inverter and the I^2t derating curve of Figure 55 are considered.

The following scenarios are possible:

- **Case1: IPeak < ICon and TempJnc < Temp1**

Both linear and I^2t derating are inactive. Maximum current is limited by system defined boundary IMax.

- **Case2: IPeak < ICon and TempJnc > Temp1**

Linear derating is active. Maximum current is limited by allowed current due to linear derating alone.

- **Case3: IPeak > ICon and TempJnc < Temp1**

I^2t Derating is active. Maximum current is limited by allowed current due to I^2t derating alone.

- **Case4: IPeak > ICon and TempJnc > Temp1**

Both linear and I^2t derating are active. Maximum current is limited by minimum of allowed current resulting from linear and I^2t derating.

For the analysis, the speed profile of **Figure 57** is used.

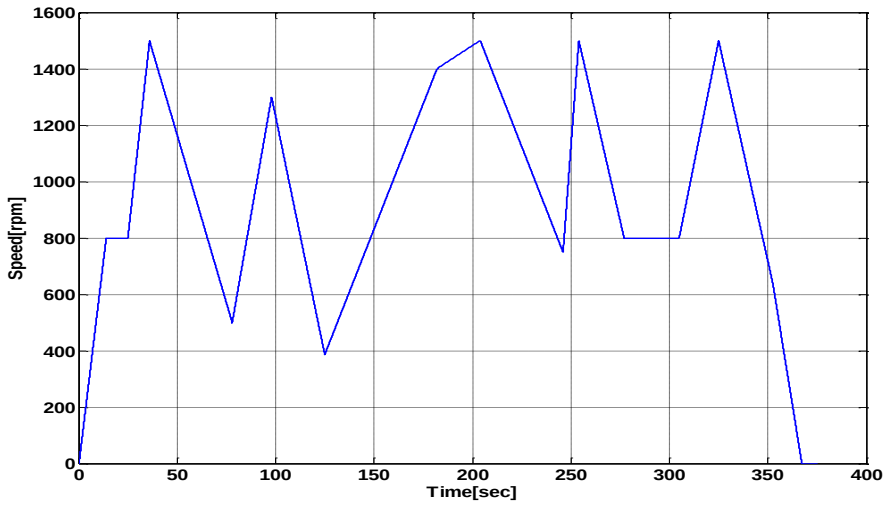

Figure 57: Traction drive speed profile

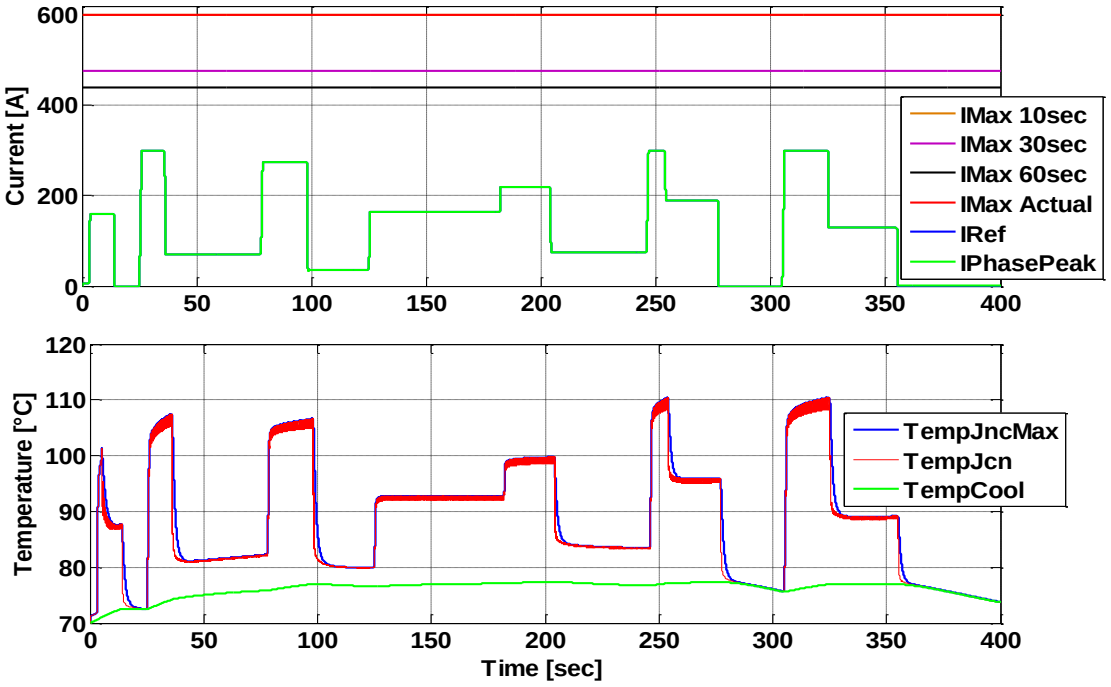

Figure 58: predictive derating case1

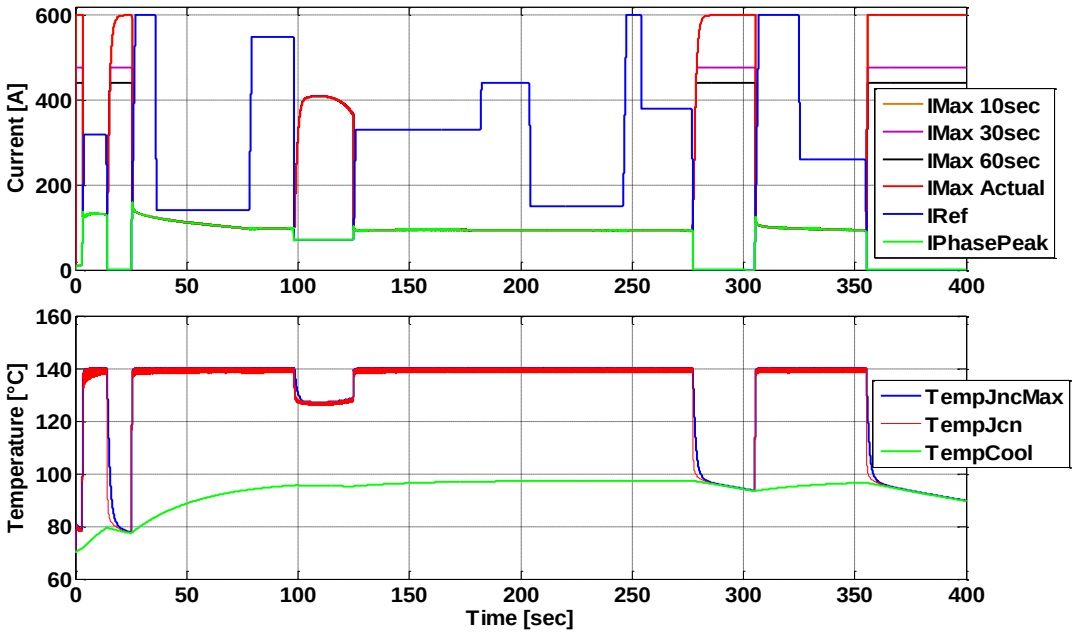

Figure 59: predictive derating case2

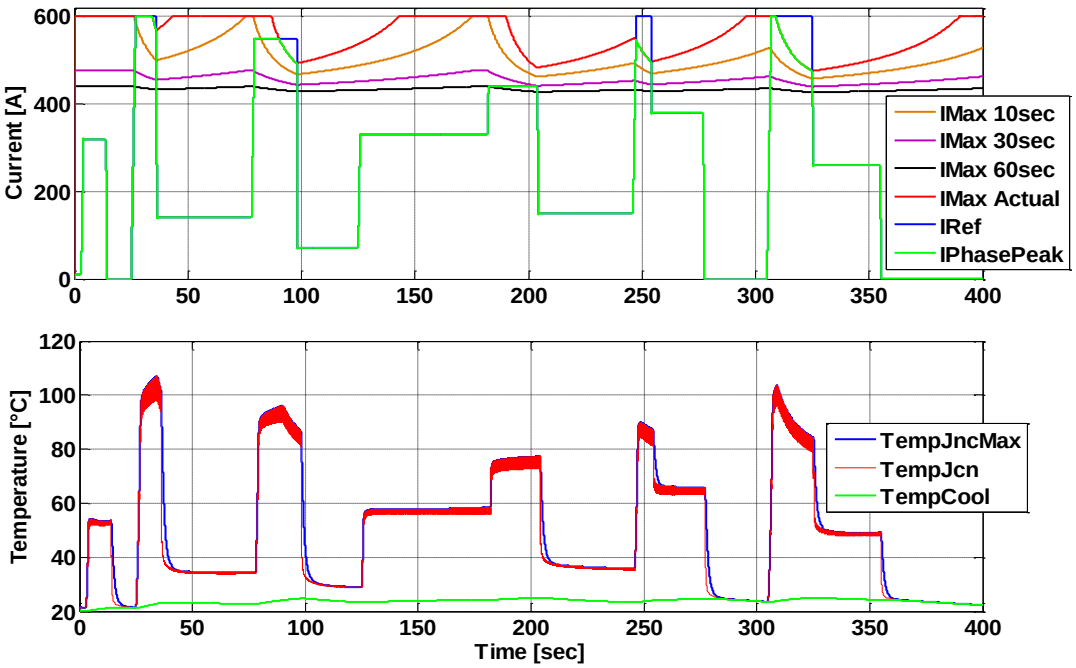

Figure 60: predictive derating case3

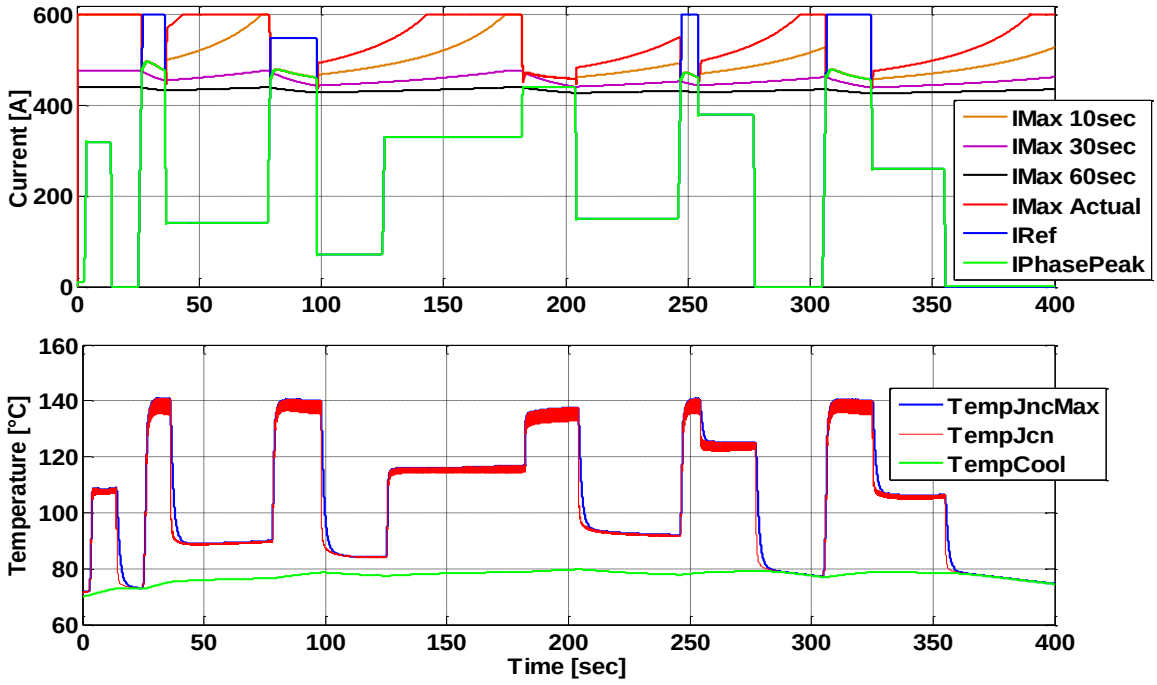

Figure 61: predictive derating case4

7. Summary and Conclusion

IGBT module temperature measurement methods using three different approaches; direct temperature measurements, voltage-based temperature measurements and infrared temperature measurements has been presented. Thermal impedance values for IGBTs and diodes for air cooled modules under different coolant air flowrates have been evaluated. The measured temperatures and the corresponding thermal impedances calculated from measured temperatures using the voltage based approach are validated with those obtained from infrared measurements. Thermal impedances for both active and passive switching elements which are necessary for a detailed thermal characterization of the IGBT module have been determined. It is observed that the difference between the average temperatures of IGBTs and diodes measured using all three methods under the same operating conditions (thermal load and coolant air flowrate) are within an acceptable margin. A 6°C and 8°C temperature difference is observed between measured average IGBT and diode temperatures respectively, using direct and voltage based methods compared to those obtained from infrared measurements which causes the corresponding thermal impedances obtained from average infrared temperatures to be higher. Significant difference between average and maximum junction temperatures of IGBT and diodes accounts for higher Zth values obtained using maximum junction temperatures measured by the infrared camera. This leaves the engineer with the choice to implement the thermal model and corresponding thermal management strategy of the inverter using either the thermal impedances from maximum or average junction temperature for the given application. Thermal management strategies using Zth values based on maximum measured junction temperatures are much more suited for applications with frequent high thermal loading of the inverter but could limit thermal performance of inverters in applications where the inverter is not frequently operated in high temperature regions in which case Zth values obtained from average measured junction temperatures suitable.

We compared the quality of prediction of the temperature of all elements in a power module using direct temperature measurements. We have shown that coefficients of the linear transfer function from the power input to the temperature can be estimated by the least squares methods with ridge regression. For a well-chosen penalization, the proposed method provided more accurate results than the industry-standard TSEP method. We have tested two models of the power input, one based on measurement of voltage drop and the second based on estimating coefficients of the second order approximation of the power from the current. Both power models achieved comparable accuracy. The proposed method is accurate and simple to use when direct temperature measurements are available.

From the thermal impedances and the switching and conduction loss parameters from the manufacturer datasheet, a thermal model for estimating the junction temperature of the inverter is implemented. Using the estimated junction temperature, an adaptive derating strategy for optimum thermal operation of an inverter in an electric drivetrain is derived. The proposed derating strategy accounts for optimal thermal

protection of the drivetrain (inverter and cables), especially at low coolant flow rates where temperature increase is very fast and only very little amounts of currents are needed to drive the inverter to temperatures close to or above the maximum allowed operating junction temperature. At high coolant flow rates or very coolant low temperatures where very high currents are needed to cause the junction temperature to increase to a critical level, the strategy also protects the cables from overheating, which could accelerate the aging or destroy the insulation. Further the proposed strategy enables the system to operate at maximum possible torque during derating without exceeding the limits of the maximum operating junction temperature. The proposed strategy also allows for smooth torque reduction in derating without drivetrain oscillation as opposed to the case with instantaneous derating. The adaptive derating strategy is an attractive candidate for commercial automotive applications as it is simple, robust, less computational intensive and can easily be implemented on a microcontroller.

References

[1] D. Blackburn, "Temperature measurements of semiconductor devices - a review," in *Twentieth Annual IEEE Semiconductor Thermal Measurement and Management Symposium* , San Jose, CA, USA, 2004.

[2] H. Niu and R. D. Lorenz, "Sensing IGBT junction temperature using gate drive output transient properties," in *IEEE Applied Power Electronics Conference and Exposition (APEC)*, Charlotte, NC, USA, 2015.

[3] H. M. N. Achiri, V. Smidl and Z. Peroutka, "Mitigation of electric drivetrain oscillation resulting from abrupt current derating at low coolant flow rate," in *41st Annual Conference of the IEEE Industrial Electronics Society*, Yokohama, 2015.

[4] H. Huang and P. A. Mawby, "A Lifetime Estimation Technique for Voltage Source Inverters," *IEEE Transactions on Power Electronics,* vol. 28, no. 8, pp. 4113 - 4119, 2013.

[5] U.-M. Choi, F. Blaabjerg and S. Jørgensen, "Study on Effect of Junction Temperature Swing Duration on Lifetime of Transfer Molded Power IGBT Modules," *IEEE Transactions on Power Electronics* , vol. 32, no. 8, pp. 6434 - 6443, 2017.

[6] S.-H. Tran, Z. Khatir, R. Lallemand, A. Ibrahim, J.-P. Ousten, J. Ewanchuk, Member, IEEE and S. V. Mollov, "Constant ΔTj Power Cycling Strategy in DC Mode for Top-Metal and Bond-Wire Contacts Degradation Investigations," *IEEE Transactions on Power Electronics,* vol. 34, no. 3, pp. 2171 - 2180, 2019.

[7] H. Chen, B. Ji, V. Pickert and W. Cao, "Real-Time Temperature Estimation for Power MOSFETs Considering Thermal Aging Effects," *IEEE Transactions on Device and Materials Reliability,* vol. 14, no. 1, pp. 220 - 228, 2013.

[8] P. Asimakopoulos, K. Papastergiou, T. Thiringer and G. L. Godec, "On Vce Method: In Situ Temperature Estimation and Aging Detection of High-Current IGBT Modules Used in Magnet Power Supplies for Particle Accelerators," *IEEE Transactions on Industrial Electronics,* vol. 66, no. 1, pp. 551 - 560, 2018.

[9] K. Vogel, A. Ciliox and A. Schmal, "IGBT with higher operation temperature - Power density, lifetime and impact on inverter design," in *PCIM Europe*, Nuremberg, 2011.

[10] M. Musallam, C. Buttay, M. Whitehead and M. Johnson, "Real-time compact electronic thermal modelling for health monitoring," in *European Conference on Power Electronics and Applications*, Aalborg, 2007.

[11] D. Murdock, J. Torres, J. Connors and R. Lorenz, "Active thermal control of power electronic modules," *IEEE Transactions on Industry Applications* , vol. 42, no. 2, pp. 552 - 558, 2006 .

[12] M. Musallam, P. Acarnley, C. Johnson, L. Pritchard and V. Pickert, "Estimation and control of power electronic device temperature during operation with variable conducting current," *IET Circuits, Devices & Systems,* vol. 1, no. 2, pp. 111 - 116, 2007.

[13] E. A. Grunditz and T. Thiringer, "Performance Analysis of Current BEVs Based on a Comprehensive Review of Specifications," *IEEE Transactions on Transportation Electrification,* vol. 2, no. 3, pp. 270 - 289 , 2016.

[14] T. Kimura, R. Saitou, K. Kubo, K. Nakatsu, H. Ishikawa and K. Sasaki, "High-power-density Inverter Technology for Hybrid and Electric Vehicle Applications," Hitachi, 2014.

[15] V. Smet, F. Forest and J.-J. Huselstein, "Ageing and Failure Modes of IGBT Modules in High-Temperature Power Cycling," *IEEE Transactions on Industrial Electronics,* vol. 58, no. 10, pp. 4931 - 4941 , 2011.

[16] J. Biela, M. Schweizer and S. Waffler, "SiC versus Si—Evaluation of Potentials for Performance Improvement of Inverter and DC–DC Converter Systems by SiC Power Semiconductors," *IEEE Transactions on Industrial Electronics* , vol. 58, no. 7, pp. 2872 - 2882 , 2011.

[17] B. Ozpineci, L. Tolbert and S. Islam, "Silicon carbide power device characterization for HEVs," in Power Electronics in Transportation," in *Power Electronics in Transportation,* Auburn Hills, 2002.

[18] B. Wrzecionko, J. Biela and J. Kolar, "SiC power semiconductors in HEVs: Influence of junction temperature on power density, chip utilization and efficiency," in *35th Annual Conference of IEEE Industrial Electronics*, Porto, 2009.

[19] Infineon, *HybridPACK 2 module with trench/fieldstop IGBT³ and Emitter Controlled diode,* 2011.

[20] Infineon, *Technical information FS400R12A2T4,* 2012.

[21] SEMIKRON, *Trench IGBT Modules SKiM306GD12E4,* 2013.

[22] S. K. Waye, S. Narumanchi, M. Mihalic, G. Moreno, K. Bennion and J. Jeffers, "Advanced liquid cooling for a traction drive inverter using jet impingement and microfinned enhanced surfaces," in *ITherm* , Orlando, 2014.

[23] Y. Yu, T.-Y. T. Lee and V. A. Chiriac, "Compact Thermal Resistor-Capacitor-Network Approach to Predicting Transient Junction Temperatures of a Power Amplifier Module," *IEEE Transactions on Components, Packaging and Manufacturing Technology ,* vol. 2, no. 7, pp. 1172 - 1181, 2012.

[24] K. Gorecki and J. Zarebski, "Nonlinear Compact Thermal Model of Power Semiconductor Devices," *IEEE Transactions on Components and Packaging Technologies,* vol. 33, no. 3, pp. 643 - 647, 2010.

[25] J. Sofia, "Analysis of thermal transient data with synthesized dynamic models for semiconductor devices," *IEEE Transactions on Components, Packaging, and Manufacturing Technology,* vol. 18, no. 1, pp. 39 - 47, 1995 .

[26] M. Rencz and V. Szekely, "Dynamic thermal multiport modeling of IC packages," *IEEE Transactions on Components and Packaging Technologies,* vol. 24, no. 4, pp. 596 - 604, 2001.

[27] Z. Wang and W. Qiao, "An Online Frequency-Domain Junction Temperature Estimation Method for IGBT Modules," *IEEE Transactions on Power Electronics,* vol. 30, no. 9, pp. 4633 - 4637, 2015.

[28] T. K. Gachovska, B. Tian, J. L. Hudgins, W. Qiao and J. F. Donlon, "A Real-Time Thermal Model for Monitoring of Power Semiconductor Devices," *IEEE Transactions on Industry Applications,* vol. 51, no. 4, pp. 3361 - 3367, 2015.

[29] M. A. Eleffendi and C. M. Johnson, "Application of Kalman Filter to Estimate Junction Temperature in IGBT Power Modules," *IEEE Transactions on Power Electronics (Volume:31 , Issue: 2),* vol. 31, no. 2, pp. 1576 - 1587, 2015.

[30] F. Filicori and C. G. L. Bianco, "A simplified thermal analysis approach for power transistor rating in PWM-controlled DC/AC converters," *IEEE Transactions on Circuits and Systems I: Fundamental Theory and Applications,* vol. 45, no. 5, pp. 557 - 566, 1998.

[31] Z. Luo, H. Ahn and M. A. E. Nokali, "A thermal model for insulated gate bipolar transistor module," *IEEE Transactions on Power Electronics,* vol. 19, no. 4, pp. 902 - 907, 2004.

[32] C.-S. Yun, P. Malberti, M. Ciappa and W. Fichtner, "Thermal component model for electrothermal analysis of IGBT module systems," *IEEE Transactions on Advanced Packaging ,* vol. 24, no. 3, pp. 401 - 406, 2001.

[33] A. Raciti and D. Cristaldi, "Thermal modeling of integrated power electronic modules by a lumped-parameter circuit approach," in *AEIT Annual Conference,* 2013, 2013.

[34] Z. Khatir, S. Carubelli and F. Lecoq, "Real-time computation of thermal constraints in multichip power electronic devices," *IEEE Transactions on Components and Packaging Technologies,* vol. 27, no. 2, pp. 337 - 344, 2004.

[35] N. Kerstin and M. Schulz, "Challenge of accurately analyzing thermal resistances," in *PCIM Europe,* Nuremberg, 2014.

[36] Y. Avenas, L. Dupont and Z. Khatir, "Temperature Measurement of Power Semiconductor Devices by Thermo-Sensitive Electrical Parameters—A Review," *IEEE Transactions on Power Electronics,* vol. 27, no. 6, pp. 3081 - 3092, 2011.

[37] M. J. Whitehead and C. M. Johnson, "Junction Temperature Elevation as a Result of Thermal Cross Coupling in a Multi-Device Power Electronic Module," in *1st Electronics Systemintegration Technology Conference,* Dresden, 2006.

[38] K. Okubo, M. Masuda, Y. Kato and Y. Nakatani, "Development of Low-loss Inverters for Electric Vehicle (EV) Motors," Mitsubishi Heavy Industries Ltd., 2008.

[39] W. Cao, F. Wang and D. Jiang, "Variable Switching Frequency PWM Strategy for Inverter Switching Loss and System Noise Reduction in Electric/Hybrid Vehicle Motor Drives," in *2013 Twenty-Eighth Annual IEEE Applied Power Electronics Conference and Exposition (APEC)*, Long Beach, CA, 2013.

[40] K. Etzold, T. Fahrbach, S. Klein, R. Scheer, D. Guse and M. Klawitter, "Function Development With an Electric-Machine-in-the-Loop Setup: A Case Study," *IEEE Transactions on Transportation Electrification*, vol. 5, no. 4, pp. 1419 - 1429, 2019.

[41] C. Lazar and D. Patrascu, *Optimal Operation of a Hybrid Electric Vehicle Based on the Prediction of the Torque and Power Availabilities,* Gheorghe Asachi Technical University of Iași, 2014.

[42] N. Amann, J. Böcker and F. Prenner, "Active Damping of Drive Train Oscillations for an Electrically Driven Vehicle," *IEEE/ASME TRANSACTIONS ON MECHATRONICS,* vol. 9, no. 4, pp. 697 - 700, 2004.

[43] S. Gay and M. Ehsani, "Impact of electric motor field-weakening on drive train oscillations," in *IEEE International Electric Machines and Drives Conference*, Madison, 2003.

[44] A. Sayed, D. Aliprantis, L. Wu, G. Zhou and S. Dutta, "Mitigation of DC-Link Voltage Oscillations Caused by Resolver Error in an Electric Vehicle Drivetrain," in *IEEE Energy Conversion Congress and Exposition (ECCE)*, Portland, 2018.

[45] T. Ohmi, Y. Abe, H. Kobayashi, K. Kondo and T. Iwasaki, "Suppression control of continuous oscillation of electric system during light-load regeneration brake control of DC electric vehicle," in *23rd International Conference on Electrical Machines and Systems (ICEMS)*, Hamamatsu, 2020 .

[46] S. Chaturvedi, R. R. Makineni, D. M. Fulwani and S. K. Yadav, "Regulation of Electric Vehicle Speed Oscillations Due to Uneven Drive Surfaces Using ISMDTC," *IEEE TRANSACTIONS ON VEHICULAR TECHNOLOGY*, vol. 70, no. 12, pp. 12506 - 12516, 2021.

[47] F. U. Syed, M. L. Kuang and H. Ying, "Active Damping Wheel-Torque Control System to Reduce Driveline Oscillations in a Power-Split Hybrid Electric Vehicle," *IEEE TRANSACTIONS ON VEHICULAR TECHNOLOGY,* vol. 58, no. 9, pp. 4769 - 4785, 2009.

[48] Z. Fu, "Real-time prediction of torque availability of an IPM synchronous machine drive for hybrid electric vehicles," in *2005 IEEE International Conference on Electric Machines and Drives*, San Antonio, 2005.

[49] H. M. N. Achiri, L. Streit, V. Smidl and Z. Peroutka, "Experimental validation of IGBT thermal impedances from voltage-based and direct temperature measurements," in *Annual Conference of the IEEE Industrial Electronics Society*, Florence, 2016.

[50] H. Njawah Achiri, V. Smidl, Z. Peroutka and L. Streit, "Least Squares Method for Identification of IGBT Thermal Impedance Networks Using Direct Temperature Measurements," *Energies*, vol. 13, no. 14, p. 3749, 2020.

[51] O. Senturk, L. Helle, S. Munk-Nielsen, P. Rodriguez and R. Teodorescu, "Converter Structure-Based Power Loss and Static Thermal Modeling of The Press-Pack IGBT Three-Level ANPC VSC Applied to Multi-MW Wind Turbines," *IEEE Transactions on Industry Applications*, vol. 47, no. 6, pp. 2505 - 2515, 2011.

[52] K. Takao and H. Ohashi, "Accurate Power Circuit Loss Estimation Method for Power Converters With Si-IGBT and SiC-Diode Hybrid Pair," *IEEE Transactions on Electron Devices*, vol. 60, no. 2, pp. 606 - 612, 2013.

[53] A. Wintrich, U. Nicolai, W. Tursky and T. Reimann, *Application Manual Power Semiconductors*, SEMIKRON International GmbH, 2011.

[54] R. Alvarez, S. Bernet, L. Lindenmueller and F. Filsecker, "Characterization of a new 4.5 kV press pack SPT+ IGBT in Voltage Source Converters with clamp circuit," in *IEEE International Conference on Industrial Technology (ICIT)*, Vi a del Mar, 2010.

[55] H. M. N. Achiri, "Design of a 100kW Traction Inverter for a Battery Electric Vehicle," University of West Bohemia, Pilsen, 2014.

[56] Infeneon, *Thermal equivalent circuit models*, 2008.

[57] ABB, *Thermal design and temperature ratings of IGBT modules*, 2013.

[58] SEMIKRON, *Thermal resistance of IGBT Modules - specification and modelling*, 2014.

[59] R. P. Stout, "Thermal RC Ladder Networks," On Semiconductor, 2006.

[60] Infineon, Transient thermal measurements and thermal equivalent circuit models, Infineon, 2020.

[61] M. N. Touzelbaev, J. Miler, Y. Yang, G. Refai-Ahmed and K. E. Goodson, "High-Efficiency Transient Temperature Calculations for Applications in Dynamic Thermal Management of Electronic Devices," *Journal of Electronic Packaging* , vol. 135, pp. 031001-1 to 031001-8, 2013.

[62] L. Dupont and Y. Avenas, "Preliminary Evaluation of Thermo-Sensitive Electrical Parameters Based on the Forward Voltage for Online Chip Temperature Measurements of IGBT Devices," *IEEE Transactions on Industry Applications* , vol. 51, no. 6, pp. 4688 - 4698, 2015.

[63] N. Baker, M. Liserre, L. Dupont and Y. Avenas, "Improved Reliability of Power Modules: A Review of Online Junction Temperature Measurement Methods," *IEEE Industrial Electronics Magazine* , vol. 8, no. 3, pp. 17 - 27, 2014.

[64] F. Yang, E. Ugur and B. Akin, "Evaluation of Aging's Effect on Temperature-Sensitive Electrical Parameters in SiC mosfets," *IEEE Transactions on Power Electronics* , vol. 35, no. 6, pp. 6315 - 6331, 2019.

[65] L. Shao, G. Xu and P. Li, "A Hybrid Model of Turn-Off Loss and Turn-Off Time for Junction Temperature Extraction," *IEEE Journal of the Electron Devices Society,* vol. 10, pp. 3 - 12, 2021.

[66] J. O. Gonzalez, O. Alatise, J. Hu, L. Ran and P. A. Mawby, "An Investigation of Temperature-Sensitive Electrical Parameters for SiC Power MOSFETs," *IEEE Transactions on Power Electronics,* vol. 32, no. 10, pp. 7954 - 7966, 2017.

[67] Q. Zhang and P. Zhang, "An Online Junction Temperature Monitoring Method for SiC MOSFETs Based on a Novel Gate Conduction Model," *IEEE Transactions on Power Electronics,* vol. 36, no. 10, pp. 11087 - 11096, 2021.

[68] H. Luo, W. Li, F. Iannuzzo, X. He and F. Blaabjerg, "Enabling Junction Temperature Estimation via Collector-Side Thermo-Sensitive Electrical Parameters Through Emitter Stray Inductance in High-Power IGBT Modules," *IEEE Transactions on Industrial Electronics,* vol. 65, no. 6, pp. 4724 - 4738, 2018.

[69] A. Arya, A. Chanekar, P. Deshmukh, A. Verma and S. Anand, "Accurate Online Junction Temperature Estimation of IGBT Using Inflection Point Based Updated I–V Characteristics," *IEEE Transactions on Power Electronics,* vol. 36, no. 9, pp. 9826 - 9836, 2021.

[70] H. M. N. Achiri, L. Streit, V. Smidl and Z. Peroutka, "Experimental Validation of IGBT Thermal Impedances from Voltage-based and Direct Temperature Measurements," in *42nd Annual Conference of the IEEE Industrial Electronics Society,* Florence, 2016.

[71] R. Schmidt and U. Scheuermann, "Using the chip as a temperature sensor — The influence of steep lateral temperature gradients on the Vce(T)-measurement," in *13th European Conference on Power Electronics and Applications*, Barcelona, 2009.

[72] L. Dupont, Y. Avenas and P.-O. Jeannin, "Comparison of Junction Temperature Evaluations in a Power IGBT Module Using an IR Camera and Three Thermosensitive Electrical Parameters," *IEEE Transactions on Industry Applications,* vol. 49, no. 4, pp. 1599 - 1608, 2013.

[73] A. E. Hoerl and R. W. Kennard, "Ridge regression: Biased estimation for nonorthogonal problems," *Technometrics,* vol. 12, no. 1, pp. 55 - 67, 1970.

[74] C. Bishop, Pattern recognition and machine learning, Volume 1, vol. 1, New York: Springer, 2006.

[75] R. Tibshirani, "Regression shrinkage and selection via the lasso," *Journal of the Royal Statistical Society: Series B (Methodological),* vol. 58, no. 1, p. 267–288, 1996.

[76] M. E. Tipping, "Sparse Bayesian Learning and the Relevance Vector Machine," *Journal of Machine Learning Research,* vol. 1, pp. 211 - 244, 2001.

[77] O. Wallscheid and J. Böcker, "Derating of automotive drive systems using model predictive control," in *IEEE International Symposium on Predictive Control of Electrical Drives and Power Electronics (PRECEDE)*, Pilsen, 2017.

[78] Schneider Electric, "Sizing and protection of conductors," 2008.

[79] T. K. Gachovska, B. Tian, J. L. Hudgins, W. Qiao and J. F. Donlon, "A Real-Time Thermal Model for Monitoring of Power Semiconductor Devices," *IEEE Transactions on Industry Applications* , vol. 51, no. 4, pp. 3361 - 3367, 2015.

[80] M. A. Eleffendi and C. M. Johnson, "Application of Kalman Filter to Estimate Junction Temperature in IGBT Power Modules," *IEEE Transactions on Power Electronics*, vol. 31, no. 2, pp. 1576 - 1587, 2016.